PHYSICAL REVIEW A VOLUME 35, NUMBER 1 JANUARY 1, 1987

Wave-vector field of convective flow patterns

M. S. Heutmaker and J. P. Gollub
Department of Physics, Haverford College, Haverford, Pennsylvania 19041-1392
and Department of Physics, University of Pennsylvania, Philadelphia, Pennsylvania 19104-6396
(Received 31 July 1986)

Textured convective flow patterns in a large cylindrical layer are studied using digital image processing methods to measure the wave-vector field $\mathbf{q}(\mathbf{r})$, a slowly varying two-dimensional field that may be used to characterize complex patterns quantitatively. We describe in some detail the development of this method and its application to the analysis of both steady and time-dependent patterns. The variation of the convective textures with $\epsilon=(R-R_c)/R_c$, where R_c is the critical Rayleigh number, is studied using quantities derived from the wave-vector field, such as its divergence and its orientation at the boundary of the container. We also find a useful criterion for the stability of convective patterns: Time-dependent patterns usually have a distribution of wave numbers that lies partially outside the predicted stable band for an infinite layer. Measurements of the Swift-Hohenberg Lyapunov functional show that this quantity varies by up to 25% for different stable patterns at the same value of ϵ.

I. INTRODUCTION

In many nonlinear systems the onset of an instability leads to the formation of a spatial pattern. Rayleigh-Bénard convection is one such system that has been extensively studied both experimentally and theoretically. At the critical Rayleigh number R_c, the homogeneous state becomes unstable to a spatially periodic flow (convection rolls) at the critical wave number q_c. When $R>R_c$, convection rolls are stable in a band of wave numbers that grows with increasing distance above onset.

Experiments have shown that under most conditions, a pattern of uniform rolls is not the preferred state of the system, when the container is of sufficiently large lateral extent. (For examples, see Refs. 1—4.) Instead, the patterns are textured; they contain bent rolls and defects, and the rolls form with their axes roughly perpendicular to the sidewalls. Each pattern contains a range of roll orientations and spacings, and thus a single wave number q is not sufficient to specify the flow structure. On the other hand, a two-dimensional wave-vector field $\mathbf{q}(\mathbf{r})$ that is a slowly varying function of position can be useful in quantitatively describing the patterns.

One purpose of this paper is to describe the application of digital image analysis to the experimental measurement of the wave-vector field. Flow visualization by the deformation of a parallel light beam allows the entire pattern to be studied simultaneously, and the addition of a digital imaging system makes it possible to analyze this data quantitatively.[4–6] We show here how $\mathbf{q}(\mathbf{r})$ may be obtained from optical intensity data.

We use $\mathbf{q}(\mathbf{r})$, in conjunction with the predictions of stability theory,[7,8] to characterize stable and time-dependent regimes of pattern evolution. We have observed persistent nonperiodic time dependence near the onset of convection (see also Ref. 9) as well as far above onset. Interestingly, the measured wave-number distribution lies *below* the predicted stable wave-number range close to onset, and *above* it far from onset. The presence of wave numbers outside the stable range seems to be a precursor of persistent time dependence.

The testing of theoretical models of pattern evolution[10–14] is another area where $\mathbf{q}(\mathbf{r})$ is useful. For example, the Swift-Hohenberg model has been studied[15–17] as a possible approximate description of transient pattern evolution. It has been formulated[17] in terms of $\mathbf{q}(\mathbf{r})$, and is therefore accessible using the experimental methods described in this paper. The model has the appealing property that pattern evolution is governed by the minimization of a Lyapunov functional F, analogous to the minimization of the free energy in equilibrium systems.

By analyzing transient pattern evolution sequences, we follow the time evolution of F and compare it with the predictions of the model.[5] The evolution of F is found to be generally consistent with a monotonic decline when $\epsilon\equiv(R-R_c/R_c)$ is of order unity. The model clearly fails when ϵ is larger than about 3.0 and may also fail very close to onset. The contribution of defects to F is difficult to measure; this leads to an uncertainty that interferes with conclusive tests.

Even though the model itself is highly simplified and at best approximate, the model and the experimental methods used to test it allow a quantitative characterization of convective textures as a function of ϵ. We find that there is a well-defined statistical trend for the ϵ dependence of the spatially averaged roll bending $\langle(\nabla\cdot\mathbf{n})^2\rangle$ and the roll obliqueness $\langle\mathbf{n}\cdot\mathbf{s}\rangle$, where ϵ is the dimensionless distance above onset, $\mathbf{n}$ is the local normal to the rolls, $\mathbf{s}$ is the local normal orientation at the outer boundary of the fluid container, and the bracket indicates an ensemble average over many patterns. These trends are in accord with expectations based on the Swift-Hohenberg model, but are violated by individual patterns.

In Sec. II of this paper we describe the experimental methods, including the digital image analysis techniques we developed to measure the wave-vector field $\mathbf{q}(\mathbf{r})$. The

experimental results are presented in Sec. III; discussion and conclusions are given in Sec. IV. The presentation of results on transient evolution in this work complements Ref. 5, and some other results have been summarized in a preliminary report.[18]

II. EXPERIMENTAL METHODS

A. Convection cell and fluid

The experiments were performed in a cylindrical cell of moderately large aspect ratio. The cell radius is $L=41.7$ mm and the depth is $d=2.97$ mm; the aspect ratio is $\Gamma=L/d=14.0$. The dimensions of the cell are a compromise between several factors. A large aspect ratio is desired, but the radius of the cell cannot exceed that of the sapphire window that serves as the upper plate. Furthermore, the depth should not be so small that a large temperature difference across the layer is required. (This would violate the Boussinesq approximation that the fluid properties except for buoyancy are independent of position.) Additionally, the time required for a single run can be inconveniently long in a very large cell, since the time-scale for pattern evolution seems to grow at least as L^2.

The working fluid is water at about 70 °C, where the Prandtl number $P=\nu/\kappa=2.5$. The critical temperature difference for convection is $\Delta T_c=0.72$ °C. The natural hydrodynamic time scales are the vertical and horizontal thermal diffusion times, $\tau_v=d^2/\kappa$ and $\tau_h=L^2/\kappa$, respectively, where κ is the thermal diffusivity. In this cell these times are $\tau_v=55$ s and $\tau_h=3.0$ h. The Boussinesq approximation applies fairly well to this experiment; at $R=5R_c$ the variation of ν (the kinematic viscosity, the fluid property that changes most rapidly with temperature) across the layer depth is about 5%.

The cell is designed to provide precise temperature control as well as optical access from above; the design is shown in Fig. 1. The lower fluid boundary is a massive copper disk, polished to a mirror finish and electroplated with nickel and rhodium to resist corrosion. The upper boundary is a single-crystal sapphire disk, used because of its high thermal conductivity. (The conductivity of sapphire is about two orders of magnitude greater than that of water, and about one order of magnitude less than that of copper.) The fluid is enclosed in a Plexiglas spacer sealed between the plates by *O*-rings and silicon grease. Thin coatings of silicon grease provide a thermal link between the spacer and the upper and lower plates, in order to reduce any azimuthal nonuniformity in the thermal boundary conditions. The small copper blocks thermally anchor the stainless-steel fill tubes to the upper plate. We found that this is necessary to prevent distortion of the convection pattern from flows induced by cool fluid in the tubes (without the blocks, these tubes are approximately at room temperature). The uppermost glass cover encloses a volume of air above the cell, to reduce heat loss and suppress the convection of room air above the apparatus.

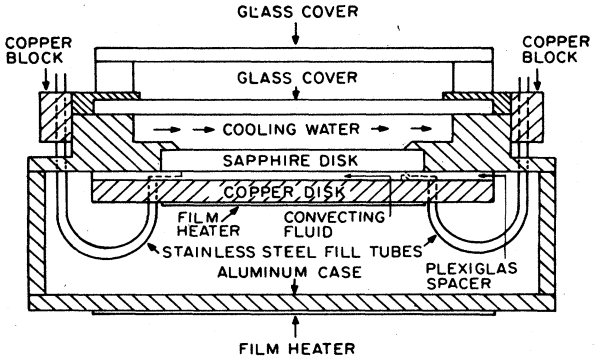

FIG. 1. Schematic diagram of the convection cell. The convecting fluid is confined between the sapphire upper plate and the copper lower plate by a plexiglas spacer.

The system contains three temperature control loops. The temperature of the lower plate is controlled by an ac feedback loop that drives a resistive film heater. The upper plate is cooled by a flow of water pumped over its upper surface from an external temperature-controlled reservoir. A commercial ac feedback controller maintains the reservoir at a fixed temperature. The lower plate is shielded from room temperature by a cylindrical case that is maintained at the mean working temperature by a commercial dc controller.

Satisfactory uniformity and long term stability in the Rayleigh number are achieved with this system. The stability of R over long times is about $\pm 0.004R_c$, and short-term fluctuations are smaller than this. The homogeneity of R is influenced by variations of the layer depth as well as those of the applied temperature difference. The thickness of the Plexiglas spacer is uniform to within about 0.5%, and this leads to variations of about 1.5% in R. This is significantly larger than the nonuniformity due to measured horizontal temperature variations.

The dimensionless distance from onset, $\epsilon=(R-R_c)/R_c$, is obviously more sensitive than R to variations in temperature and layer depth. Close to onset (at $\epsilon=0.1$), the stability of ϵ was typically $\pm 2\%$. In this worst case, the horizontal inhomogeneity in ϵ (due mostly to layer depth variations) could have been as large as 15%. These variations may be significant, and we cannot rule out the possibility that some features of the flow near onset might be different in a cell that has better uniformity of the layer depth.

B. Flow visualization and digital imaging

The convective flow is visualized using the shadowgraph technique with a laser light source, as shown in Fig. 2. The parallel expanded beam of an argon ion laser enters the cell from above, reflects from the polished lower plate, and then reflects from a beam splitter to a translucent screen. The laser provides a well-collimated beam. However, it was necessary to place a rotating translucent screen at the focus of the beam expander to eliminate troublesome speckle in the image, by reducing the coherence of the light.

As the beam passes through the convecting fluid, it is locally focused or defocused by the temperature-dependent variations in the index of refraction

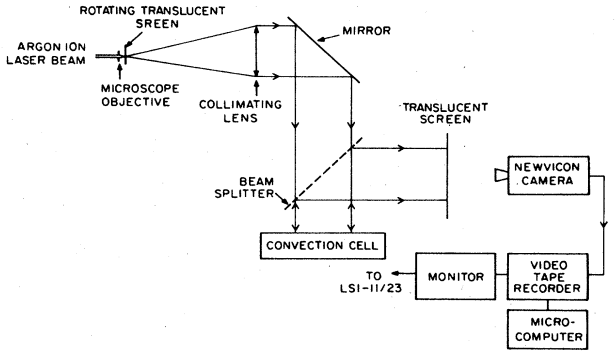

FIG. 2. Diagram of the flow visualization apparatus and image digitization equipment. Images are stored on videotape before being digitized and processed.

($dn/dT \simeq -0.0002$ K^{-1} for water at 70°C). Horizontal nonuniformity in the second spatial derivatives of the index cause nonuniform distortion of the parallel beam, and this produces contrast on a screen some distance from the cell. Cold (downflowing) areas of the fluid cause the beam to converge, and warm (upflowing) areas cause the beam to diverge; hence the fluid acts as a horizontal array of lenses. The contrast in the image increases with ϵ; for $\epsilon = 0.2$ with the screen about 1.5 m from the cell, the contrast is about 10%. A Newvicon camera is used to record the image on the screen on videotape for later digital processing.

The primary drawback of the shadowgraph technique is the difficulty of extracting hydrodynamic data, such as the (vertically averaged) temperature field, from the intensity distribution[19,20] in the image. When the screen is positioned for a sharply focused image, the data is no longer spatially invertible, since a single point on the screen receives light rays that have passed through different horizontal locations in the fluid. However, the shadowgraph images provide useful information about the spatial structure and time dependence of the pattern.

Images are digitized, stored and processed using a Digital Equipment Corporation LSI-11/23 computer with two supplementary graphics boards (manufactured by Datacube, Inc.) installed on the bus. These boards allow a video signal to be digitized with 8-bit (binary digit) accuracy and permit an image to be stored as an array of 240×320 bytes (1 byte $\equiv$ 8 bits). Software to drive and access the graphics device was written in our laboratory.

In order to analyze the shadowgraph images quantitatively, it is necessary to eliminate spatial distortions due to the digital imaging system. We found that the image of the cell was slightly stretched (less than 5%) in one direction, primarily due to spatial nonlinearity of the camera. This aberration was corrected digitially before further processing.

Frame averaging is a useful method to reduce spurious intensity variations in the digitized image.[21] Noise in the image from mis-synchronization (due to slight tape speed variations, for example) can be bothersome during subsequent processing. When the flow is changing slowly, an average of many frames is still an effectively instantaneous image. We find that summing 64 frames (this requires about $1\tau_v$) reduces the noise in the image to an acceptable level. Figure 3(a) shows a typical image after

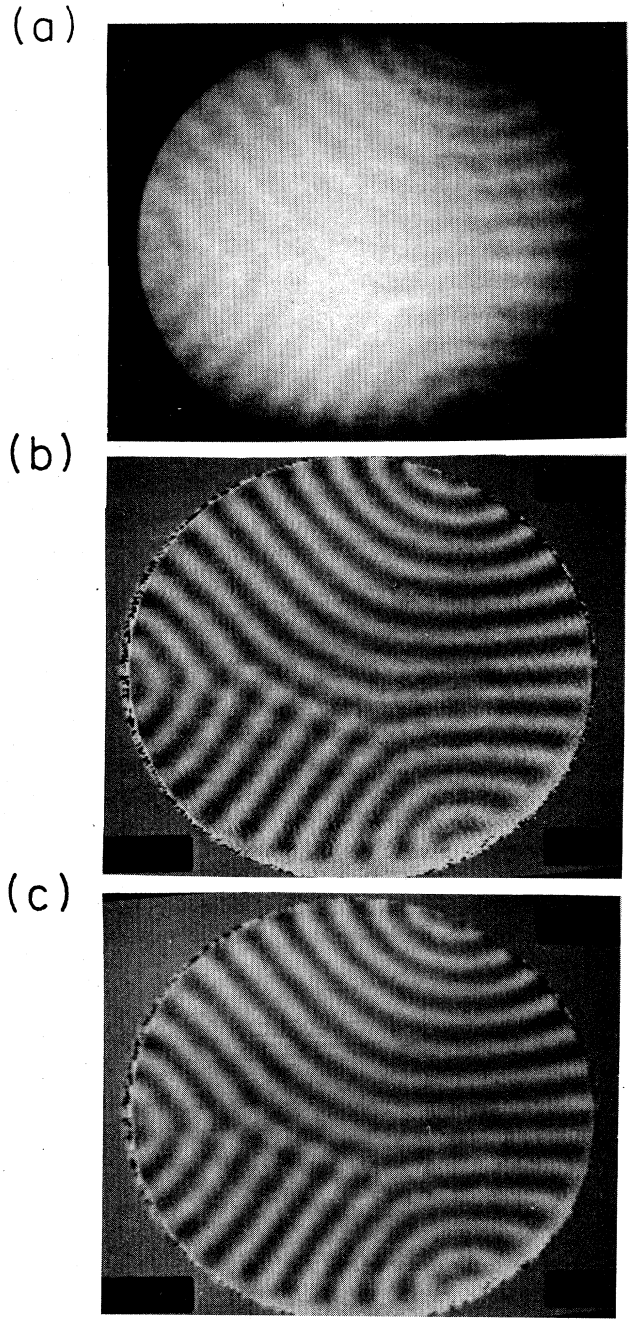

FIG. 3. Processing the shadowgraph by image division and smoothing. (a) Image (at $\epsilon = 0.1$) formed by averaging 64 video frames; the contrast is weak and the illumination nonuniform. (b) Point-by-point division by a reference image with no convection improves uniformity and allows contrast to be enhanced. (c) Nearest pixel smoothing reduces small scale noise.

averaging 64 frames, at $\epsilon=0.10$. The relatively low contrast is apparent.

Image division is then used to increase contrast in the image and to reduce the effects of nonuniform illumination and optical imperfections.[21] (This operation also increases any residual noise in the image.) Let $I(j,k)$ be the intensity in a frame-averaged image of a convection pattern and let $I_b(j,k)$ be the intensity in an averaged background image of the cell where convection is absent. Here j and k are the indices of a given picture element (pixel) in the byte array that contains the image. Then the intensity in the quotient image is

$$I'(j,k)=I_0+G\log_2[I(j,k)/I_b(j,k)]\ ,$$

where I_0 is a center intensity and the gain G is chosen to yield the desired contrast. Figure 3(b) shows the image of Fig. 3(a) after division; this image is suitable for quantitative analysis, although some enhancement of residual noise on small length scales is visible.

If necessary, small-scale residual noise in the image can be reduced with a spatial low-pass filter. The simplest way to implement this operation[21] is to average the intensity of each pixel with that of nearest-neighbor pixels. Since the minimum roll width in the image is about 7 pixels, a single application of this filter does not significantly degrade the spatial structure information in the image. Figure 3(c) shows the image of Fig. 3(b) after a single smoothing operation.

C. Measurement of the wave-vector field from shadowgraph images

Several operations are necessary to extract $\mathbf{q}(\mathbf{r})$ from shadowgraph data. The position and local orientation of roll boundaries in the image are found first. The defects in the pattern are located and marked. Then the local roll orientation and spacing are measured on a regularly spaced grid of points to find $\mathbf{q}(\mathbf{r})$. The spacing of the grid (5 pixels) is chosen to ensure that there is at least one grid point per roll width; in this case a 45×45 array of points covers the cell area. These various steps are now described in detail.

1. Digitization of roll boundaries

The position and orientation of roll boundaries in the pattern are found by following contours of maximum and minimum intensity in the image. We use an interactive graphics program to digitize the roll boundaries semiautomatically.[21,22] In operation, the user moves a cursor over the image stored in graphics memory to specify a starting point and ending point along a roll boundary. The program automatically follows the path of maximum brightness between the two points, and stores the location and orientation of points along the path in a buffer. Both dark (warm) as well as bright (cold) roll boundaries can be analyzed by inverting the intensities in the image. This digitized contour is smoothed, and the orientation calculated at each point, using a moving linear regression. After repeating this process for each roll boundary we have a digital representation of the pattern; this is stored for use in further analysis.

We have measured the accuracy of the contours found by this method.[22] Typical rms angular deviations are $\pm\pi/60$ (larger in highly curved rolls). The position of digitized contours is reproducible and accurate to within about one pixel.

2. Defects

Textured convection patterns contain a variety of defects: dislocations, disclinations and grain boundaries. The insertion of an extra roll pair into an otherwise uniform pattern forms a dislocation. Points where the orientation is singular[10] are called disclinations; e.g., at the center of a patch of circular rolls. Grain boundaries[17] form where roll patches of differing orientation are joined in a line.

The local wave vector is undefined at the defects, so it is necessary to locate the defects before $\mathbf{q}(\mathbf{r})$ can be measured. A small region around each disclination and grain boundary is excluded from the wave-vector measurement. Figure 4 shows the digitized roll boundaries and marked defects for two patterns. Figure 4(a) is the pattern of Fig. 3, and Fig. 4(b) shows a different pattern that contains a variety of defects.

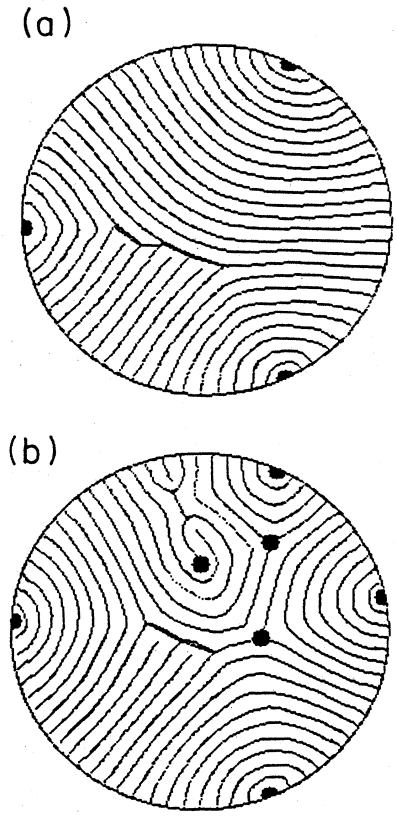

FIG. 4. Digitized roll boundaries for two patterns; (a) corresponds to the shadowgraph of Fig. 3; it contains three sidewall disclinations and a grain boundary. (b) Pattern from a different run containing four sidewall disclinations, three bulk disclinations, two dislocations, and a grain boundary.

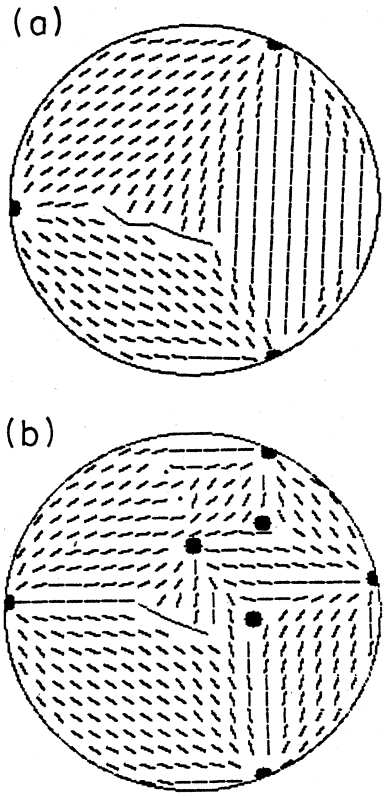

FIG. 5. Orientation field $\mathbf{n}(\mathbf{r})$ measured for the patterns of Fig. 4. The orientation perpendicular to the local roll axis is shown by the line segments.

3. *Measurement of roll orientation and spacing*

We evaluate $\mathbf{q}(\mathbf{r})$ as the product of two fields, the orientation $\mathbf{n}(\mathbf{r})$ and the wave number $q(\mathbf{r})$; these are measured in separate steps. Here $\mathbf{n}=\mathbf{q}/|\mathbf{q}|$ is a unit vector perpendicular to the roll axis.

Orientation field. The orientation is measured at each grid point by interpolation from nearby roll boundaries. The digitized roll boundaries and defects are displayed in graphics memory. At each grid point where $\mathbf{n}(\mathbf{r})$ is defined, the graphics memory is searched to locate the roll boundaries nearest the grid point. The orientations at these two boundaries are averaged (weighted by their distance from the grid point) to find $\mathbf{n}$ at the grid point. (This procedure is modified near defects and the sidewall, where the grid point does not always lie between two roll boundaries.) Tests[22] show that the accuracy of $\mathbf{n}(\mathbf{r})$ is comparable to that of the orientation of the digitized boundaries. Figure 5 shows a subset of the field $\mathbf{n}(\mathbf{r})$ measured from the digitized patterns of Fig. 4. The defects are also shown.

Wave-number field. The local wave number q is derived from the measurement of the roll spacing l, using the relationship $q=\pi/l$ (note that one roll width is half a wavelength). This method is most useful when the phase (and hence the wave number) of the structure varies slowly in space so that the measurement of only two points per half-cycle (i.e., the roll width) is sufficient to specify the wave number. In order to convert the units of q from $(\text{pixels})^{-1}$ to the physically meaningful $(\text{layer depth})^{-1}$, we multiply all length measurements by the scale factor $\Sigma=\Gamma/R$, where $\Gamma=14.0$ is the aspect ratio, and R is the radius (in pixels) of the image of the cell.

The spatial resolution of the digital imaging system is an important consideration in the measurement of the local roll width. Since the critical roll width corresponds to a length of about 7 pixels in the image, the precision of a single width measurement made by locating the digitized boundaries will be about 10% (although it improves if the roll width is larger). For some purposes this is insufficient, and below we discuss two techniques to increase the precision of the roll width measurement. In many cases these two methods yield similar results.

One method of noise reduction uses the digitized roll boundaries and the previously measured $\mathbf{n}(\mathbf{r})$. Instead of making a single measurement of the distance between the digitized roll boundaries at each grid point, we also measure the spacing at several adjacent pixels near the grid point, and these values are averaged to find l at the grid point. (The additional measurement locations are positioned to avoid overlap with measurements at the adjacent grid points.) We find an improvement of about a factor of 2 in the precision of l after averaging in this way.

A second method uses $\mathbf{n}(\mathbf{r})$ and the processed ("background-removed") shadowgraph image to find the roll spacing. Instead of searching around each grid point to locate digitized boundaries, we make a one-dimensional scan of the image intensity, centered on the grid point and parallel to $\mathbf{n}$. Once this intensity profile has been read, the locations of the roll boundaries nearest the grid point are found by fitting parabolas to the nearest minimum and maximum in the profile. Since the intensity profiles are sensitive to noise in the shadowgraph image, several steps are taken to increase the reproducibility of these profiles. First the image is smoothed, using one application of the spatial filtering operation described in Sec. II B above. Additionally, for each point in the profile (the profile is read along a line parallel to $\mathbf{n}$) the intensity is averaged over a short segment perpendicular to $\mathbf{n}$ (parallel to the roll axis).

Figure 6 shows a typical intensity profile (points) de-

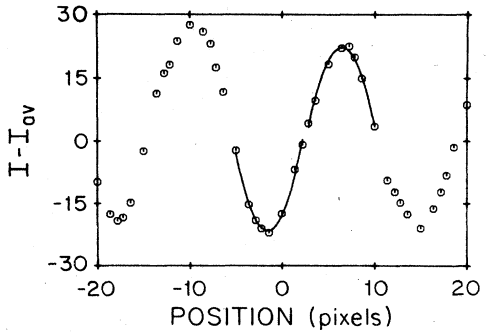

FIG. 6. Wave-number measurement by parabolic fits to intensity extrema nearest a grid point. The solid lines are fits to the peak and valley data (circles).

rived in this way from the pattern of Fig. 3(c), along with the quadratic fits (solid lines) to the peak and valley nearest the grid point. In uniform areas of patterns, this method typically[22] yields rms wave-number deviations of about $\pm 0.03 q_c$.

In Fig. 7 we show the measured wave-number field $q(\mathbf{r})$ for the two patterns of Fig. 4. The intensity of the gray scale at each grid point (represented as a solid block) is coded in proportion to the wave number. The locations of defects are indicated by the vertically striped areas.

D. Quantities derived from the wave-vector field

In addition to $\mathbf{q}(\mathbf{r})$, several other quantities are useful in the analysis of patterns. Here we discuss the measurement of some of these quantities; a more detailed discussion is presented in Ref. 22.

The wavenumber distribution $P(q)$ for a pattern can be computed easily, in histogram form, from the wave-number field $q(\mathbf{r})$. This measurement of $P(q)$ may differ from the distribution that could be calculated from a two-dimensional Fourier analysis of the pattern. However, in a pattern containing only about 10 cycles (roll pairs), the resolution of the real-space measurement is better than that of a Fourier transform.

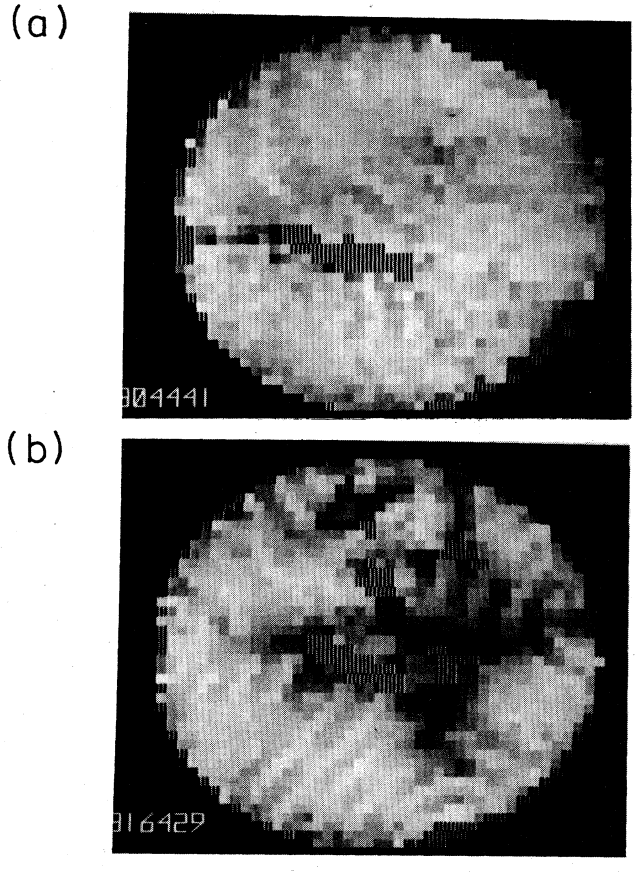

FIG. 7. Measured wave-number field $q(\mathbf{r})$ for the patterns of Fig. 4. The intensity of the grey scale is coded in proportion to the wave number; the field cannot be measured near the defects (vertically striped regions).

The "roll bending field" $(\nabla\cdot\mathbf{n})^2$ is a quantitative measure of the structure of the pattern. In a pattern of concentric rolls, $(\nabla\cdot\mathbf{n})^2 = 1/r^2$, where r is the radial coordinate. The interpretation of $(\nabla\cdot\mathbf{n})^2$ as (radius of curvature)$^{-2}$ can be applied to other patterns as well. We compute the bending from $\mathbf{n}(\mathbf{r})$ by numerical differentiation, using two-point centered differences.[23] The bending cannot be computed close to defects and the sidewall, where $\mathbf{n}(\mathbf{r})$ is not defined. In actual data, the bending is quite sensitive to errors in the measured $\mathbf{n}(\mathbf{r})$, but we estimate the precision of the spatially averaged bending $\langle(\nabla\cdot\mathbf{n})^2\rangle$ to be about $\pm 5\%$. (Here $\langle\ \rangle$ denotes an average over a single pattern.) Similar remarks apply to the squared wave-vector divergence $(\nabla\cdot\mathbf{q})^2/q_0^2$, where q_0 is a reference wave number.

Another quantity that reflects the structure of the pattern is the roll-sidewall obliqueness $\mathbf{n}\cdot\mathbf{s}$, where $\mathbf{s}$ is a unit vector perpendicular to the sidewall. This quantity is evaluated at the perimeter of the cell, and vanishes where the rolls are perpendicular to the sidewall. We take $\mathbf{n}\cdot\mathbf{s} = \cos\beta$, where β is the positive acute angle between $\mathbf{n}$ and $\mathbf{s}$. For better precision, the obliqueness is computed at every pixel on the perimeter, instead of using just the values of $\mathbf{n}(\mathbf{r})$ at grid points near the sidewall. Also, a small arclength is excluded near defects on the sidewall. In actual data we estimate the accuracy of the spatial average $\langle\mathbf{n}\cdot\mathbf{s}\rangle$ to be about $\pm 3\%$.

Most of the contributions[17] to the Lyapunov functional in the Swift-Hohenberg model can be computed easily from the wave-number field, or as integrals of quantities described above. The bulk contribution F_B consists of two terms: $F_{\delta q}$, which is proportional to the integral over the cell area of $(q-q_0)^2$, where q_0 is a reference wavenumber; and F_{div}, a quantity proportional to the integral of $(\nabla\cdot\mathbf{q})^2/q_0^2$ over the cell area. The sidewall contribution F_S is proportional to the integral of $\mathbf{n}\cdot\mathbf{s}$ around the perimeter of the cell. Further discussion of the calculation of the contributions to F may be found in Refs. 5 and 22.

III. EXPERIMENTAL RESULTS

We present the results of this study in two subsections. We begin with a qualitative overview of the observed regimes of both stable pattern formation (including transient evolution) and persistent time dependence, and then proceed to the quantitative analysis of patterns in the various regimes.

A. Overview: Three regimes of pattern evolution

We have found three regimes of pattern evolution for $\epsilon < 5$. When $\epsilon < 0.2$ or $\epsilon > 3.5$, nonperiodic time dependence appears to persist indefinitely. The time scales of the motion are much slower in the small ϵ regime. On the other hand, for $0.2 < \epsilon < 3.5$, *stable* nonunique textured patterns form after long transients. The boundaries between these regimes probably depend on the Prandtl number, and may also depend on initial conditions.

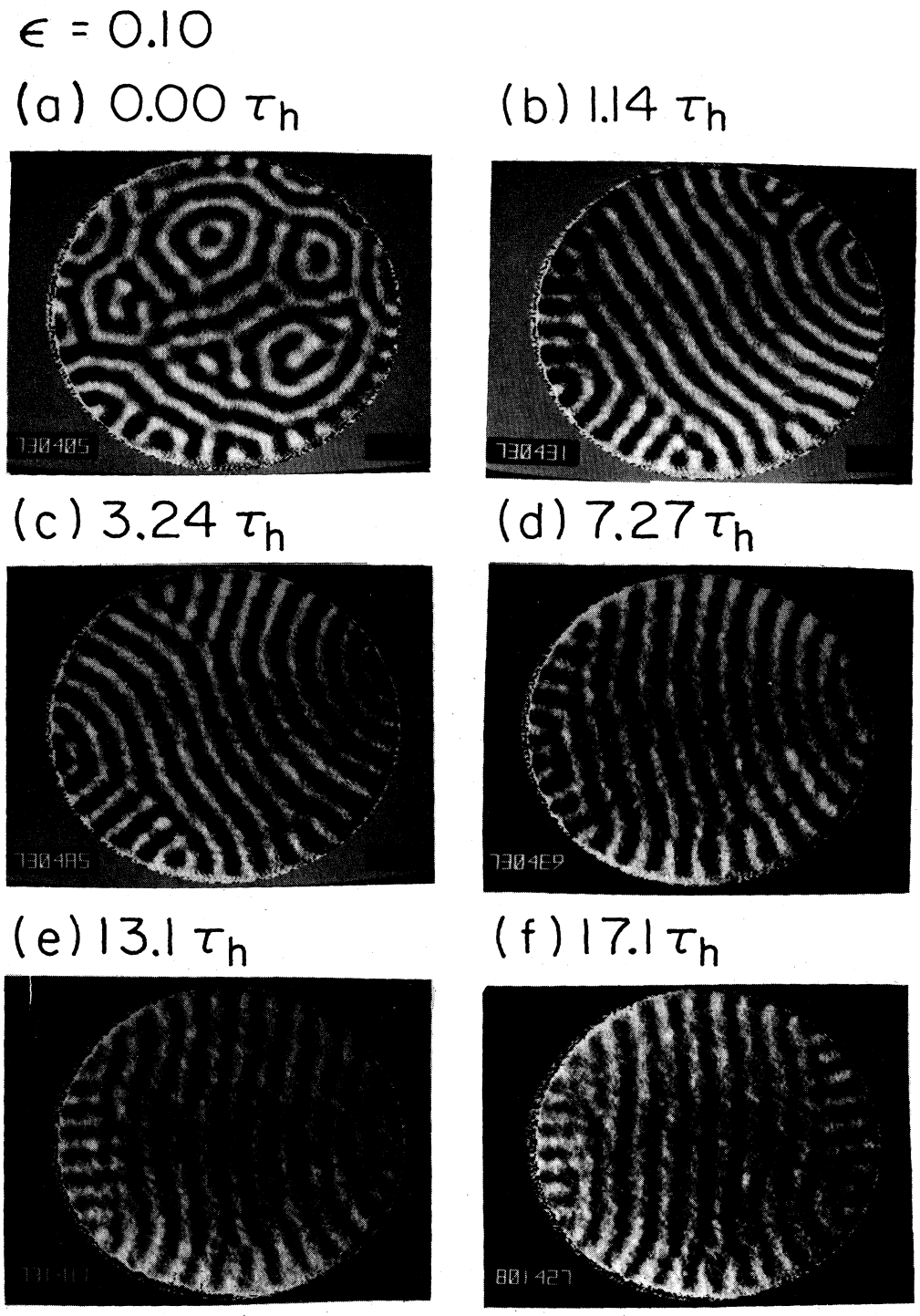

FIG. 8. Sequences of images at $\epsilon=0.10$ (10% above onset) showing persistent time dependence near the onset of convection. Times are given in units of the horizontal thermal diffusion time τ_h. Grain boundary motions persist throughout observations spanning $45\tau_h$.

1. *Time dependence close to onset*

Sufficiently close to onset, convective flows apparently do not stabilize. For $\epsilon<0.2$ (approximately), slow nonperiodic motion (on a time scale of a few τ_h) persists for at least $50\tau_h$. This motion involves the restructuring of defects, and was originally pointed out by Ahlers, Steinberg, and Cannell.[9]

An example of persistent time dependence close to onset is shown in Fig. 8, where we present a sequence of im-

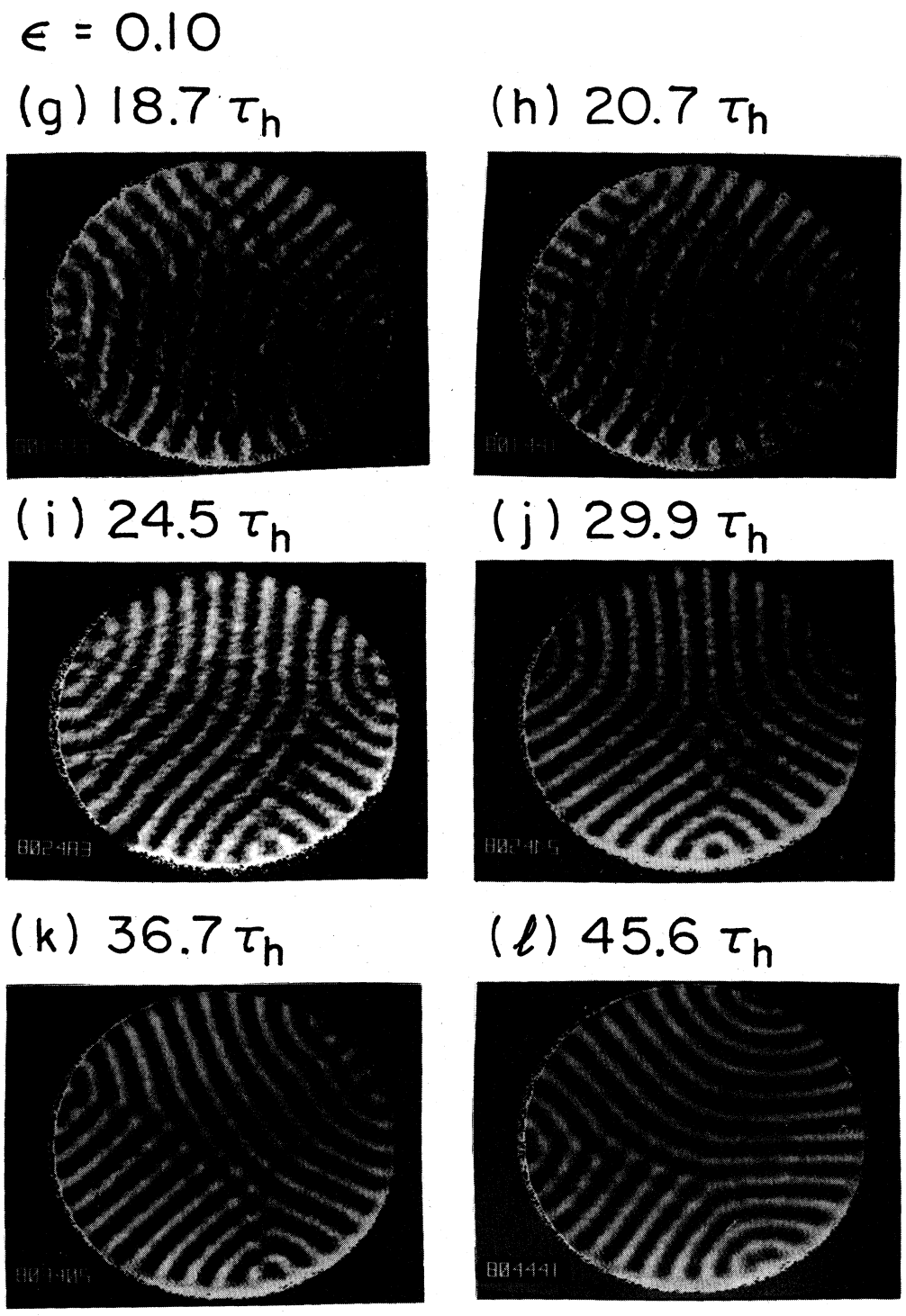

FIG. 8. (*Continued*).

ages at $\epsilon=0.10$. The time elapsed since ϵ was set to 0.10 is shown in units of τ_h. A highly disordered initial pattern [Fig. 8(a)] was created by raising ϵ rapidly through zero to a large value ($\epsilon\simeq 5$) and then setting $\epsilon=0.10$. Within about $1\tau_h$ [see Fig. 8(b)], the flow contains only a few defects and a large region of slightly bent rolls.

Instead of stabilizing, these defects evolve erratically: grain boundaries occasionally propagate around the per-

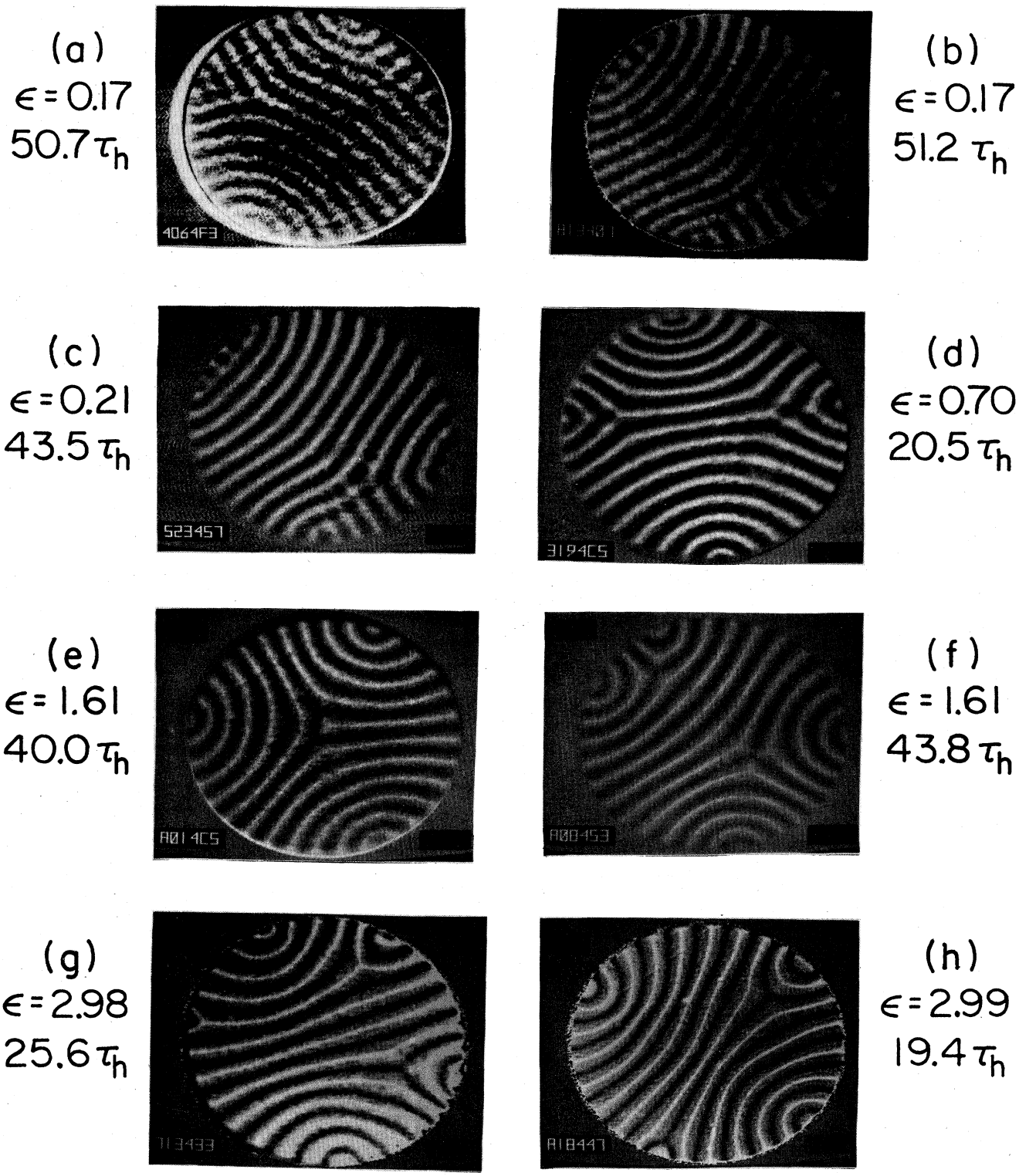

FIG. 9. Stable textured patterns formed at various ϵ. The patterns are not unique at a given ϵ: note (a) and (b); (e) and (f); and (g) and (h). The elapsed time is also shown.

imeter of the pattern (b)—(d) and (f)—(h). The motion of these defects is not restricted to the perimeter of the container. In Figs. 8(i)—8(k), a grain boundary grows out from the sidewall and eventually spans nearly the diameter of the cell. The motion of these defects shows no sign of abating during the entire time of observation ($45\tau_h$).

Although elements of this process are repetitive, the evolution is apparently nonperiodic. The phenomenon is not always as pronounced as in Fig. 8. For example, another run at the same ϵ shows weaker but still significant time dependence.

2. Stable patterns and transient evolution

For $0.2<\epsilon<3.5$ textured patterns become stable eventually, regardless of the initial conditions. Some of these are displayed in Fig. 9. They form after long transients; the elapsed time is also given for each image. We classify a pattern as stable when shifts (measured by image division) of not more than a small fraction of a roll width occur over time intervals of order $10\tau_h$. (Close to onset, the transients tend to last longer than at higher ϵ, and some of the patterns at $\epsilon<0.5$ in Fig. 9 may still be evolving very slowly.)

Several features are present in all of these flows: the rolls are bent and tend to be roughly perpendicular to the sidewall; a small number of defects are present on the sidewall and in the bulk of the pattern. The patterns are not unique at a given value of ϵ; this is shown for three values of ϵ in Figs. 9(a) and 9(b) and 9(e)—9(h).

When R_c is exceeded slowly, we have observed stable patterns consisting of concentric or elliptical rolls, over a range of ϵ similar to that for textured patterns. Patterns of this type have been thoroughly characterized[4] and we will not discuss them further.

An example of transient evolution to a stable pattern is shown in Fig. 10, at $\epsilon=1.56$. In this example, a large number of defects persist in the pattern until almost $7\tau_h$ [Fig. 10(f)], and then the few remaining defects evolve slowly until the pattern stabilizes at about $40\tau_h$. During the slow phase, a wave-number adjustment occurs [this can be seen by counting the number of rolls in the images of Figs. 10(g) and 10(h)], and a new defect pair grows out of the sidewall (i) and (j).

3. Time dependence far from onset

For ϵ sufficiently large ($\epsilon>3.5$), persistent nonperiodic time dependence occurs through repetitive pinching of the rolls. The time scale of this phenomenon is much faster than that of the persistent motion of grain boundaries at small ϵ.

An example of this process is shown in Fig. 11, at $\epsilon=3.84$; here the elapsed time (from an arbitrary initial point) is given in units of the *vertical* thermal diffusion time $\tau_v=55$ s. Figure 11(a) shows a typical time-dependent pattern, consisting largely of curved rolls between two sidewall disclinations (SD). As three new rolls [Fig. 11(b)—11(d), arrows] are added at the SD, the rolls are compressed in the center of the pattern and eventually pinch off [(e) and (f)]. This leads to the formation of a pair of dislocations (g) that quickly climb to the sidewall [(h) and (i)]. Soon new rolls (only two this time) grow from the SD again [(j) and (k)], and the process repeats [(l)].

Although these phenomena are repetitive, the events occur nonperiodically and with various spatial structures. The roll pinching is not always near the center of the pattern, and it sometimes occurs in several places simultaneously. Patterns may contain more defects than in this example, and then the flow changes are difficult to characterize.

B. Quantitative analysis

1. The form of stable patterns

Although a single wave number is not sufficient to specify the structure of a textured pattern, the spatially averaged wave number $\langle q\rangle$ (here $\langle\ \rangle$ denotes the average over a single pattern) tends to decrease with increasing ϵ. Figure 12 shows ϵ versus $\langle q\rangle/q_c$ for stable textured patterns, along with the thresholds of several secondary instabilities. The instability boundaries[8] are computed for an infinite array of straight rolls at $P=2.5$. (Here EC denotes Eckhaus, ZZ denotes zig-zag, CR denotes cross roll, and SV denotes skewed varicose.) The variations of $\langle q\rangle$ at fixed ϵ are an indication of the nonuniqueness of these patterns. Although these variations are significant, they are much smaller than the range of q predicted to be stable. It also appears that the limiting value of $\langle q\rangle$ as $\epsilon\rightarrow 0^+$ is about $0.95q_c$, instead of q_c, the value that would be expected for straight rolls.

The spatially averaged roll bending $\langle(\nabla\cdot\mathbf{n})^2\rangle$ and roll obliqueness $\langle\mathbf{n}\cdot\mathbf{s}\rangle$ also tend to vary with ϵ. Generally we find that the rolls bend more, and are more nearly perpendicular to the sidewall, as ϵ is increased. (This trend can be seen qualitatively in some of the patterns of Fig. 9.) However, the patterns *do not always* vary in this way, as will be shown below.

Figure 13(a) shows $\langle\mathbf{n}\cdot\mathbf{s}\rangle$ as a function of ϵ for a number of stable patterns (most of these evolved from complicated patterns). As ϵ increases from 0.2 to 1.6, the mean obliqueness decreases by about 30%. In textured patterns $\langle\mathbf{n}\cdot\mathbf{s}\rangle$ is always much smaller than the value of 0.64 expected for straight rolls in a circular container. On the other hand, it is never smaller than about 0.15 because the rolls do not bend sharply enough near defects to be perpendicular to the sidewall everywhere. The mean roll bending $\langle(\nabla\cdot\mathbf{n})^2\rangle$ is plotted versus ϵ in Fig. 13(b); it increases by about 80% as ϵ increases from 0.2 to 1.6. The largest measured values of $\langle(\nabla\cdot\mathbf{n})^2\rangle$ are comparable to that expected in a concentric pattern, about 0.03.

Although the bending and obliqueness vary oppositely to each other, this variation is not always monotonic with ϵ. Figure 14 shows these quantities as a function of ϵ for a sequence of patterns formed sequentially at successively higher values of ϵ. In this example, the pattern first becomes straighter (and the obliqueness increases) as ϵ is increased from 0.2; the trends at low ϵ are opposite to those of Fig. 13.

2. Wave-number field and the onset of time dependence

We find that it is useful to characterize patterns by the wave-number distribution $P(q)$, and to compare $P(q)$

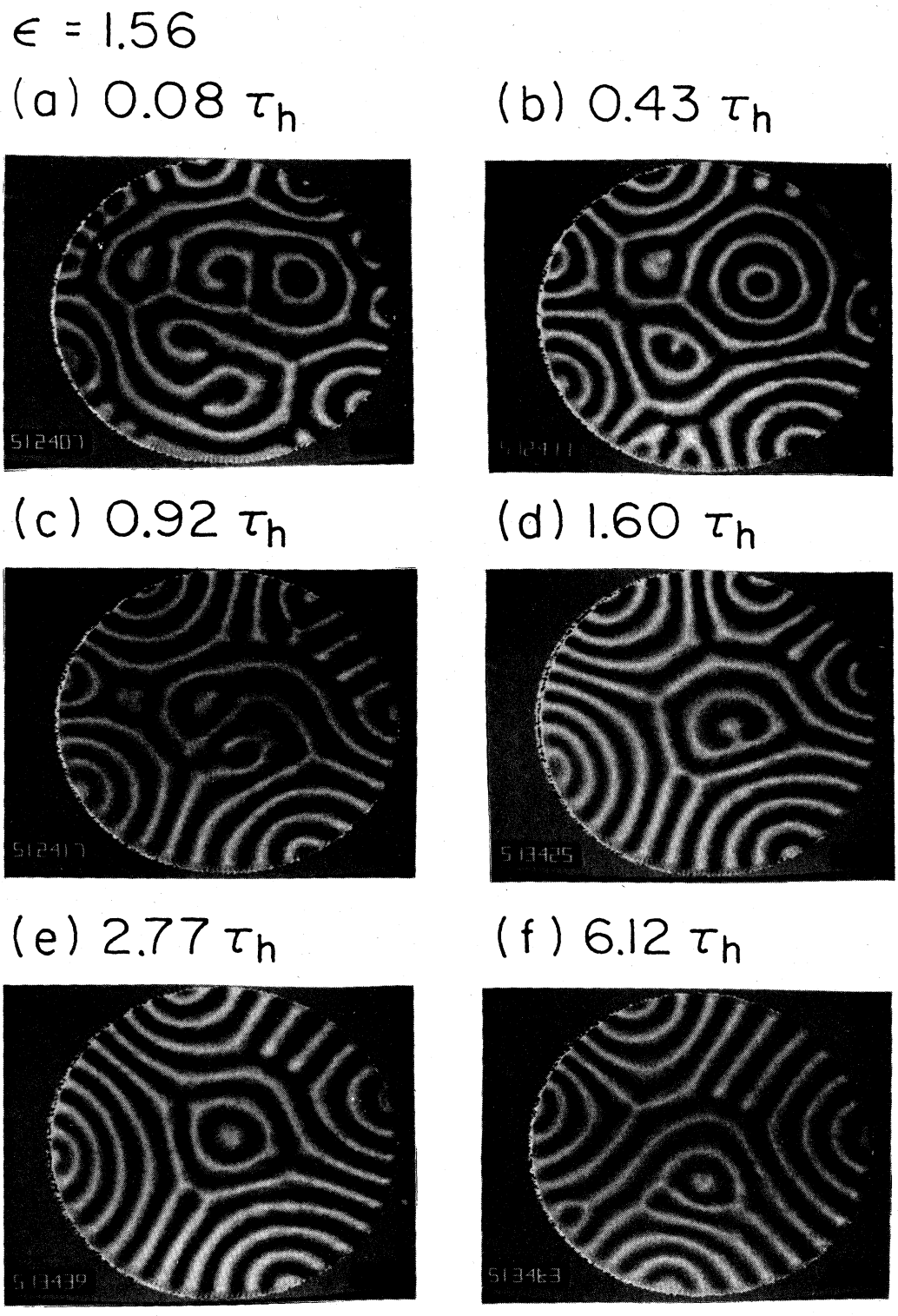

FIG. 10. Transient evolution sequence at $\epsilon = 1.56$. Large wave-number variations are visible as defects evolve.

with the predictions of stability theory. For many stable patterns, i.e., over much of the interval $0.2 < \epsilon < 3.5$, $P(q)$ lies entirely within the wave-number band expected from stability theory. However, for ϵ sufficiently small or sufficiently large, $P(q)$ exceeds the stable band and this condition seems to be a useful predictor of the onset of persistent time dependence.

This is demonstrated in Fig. 15, which shows $P(q)$ for a pattern from each of the three regimes, along with the location of the stable wave-number band. The distribu-

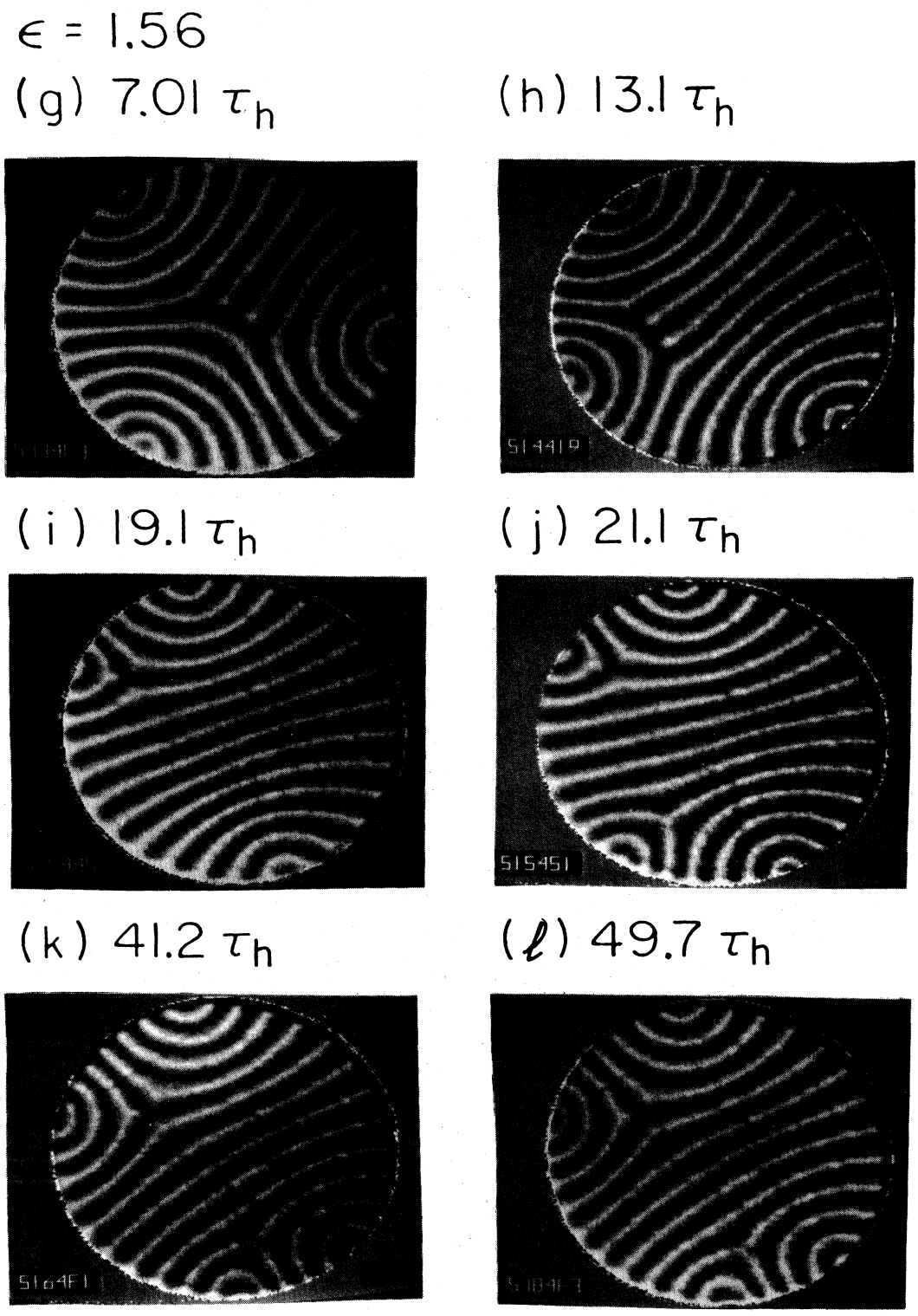

FIG. 10. (*Continued*).

tion is plotted in histogram form; the width of each bin is comparable to the resolution of the wave-number measurement. *Close* to onset [$\epsilon=0.10$, Fig. 15(a)], the pattern is time dependent and much of $P(q)$ lies *below* the stable band, below the threshold of the zig-zag (ZZ) instability. [The knot (KN) instability limits the high side of the stable band.] On the other hand, for stable patterns such as that of Fig. 15(b) at $\epsilon=1.61$, $P(q)$ lies entirely within

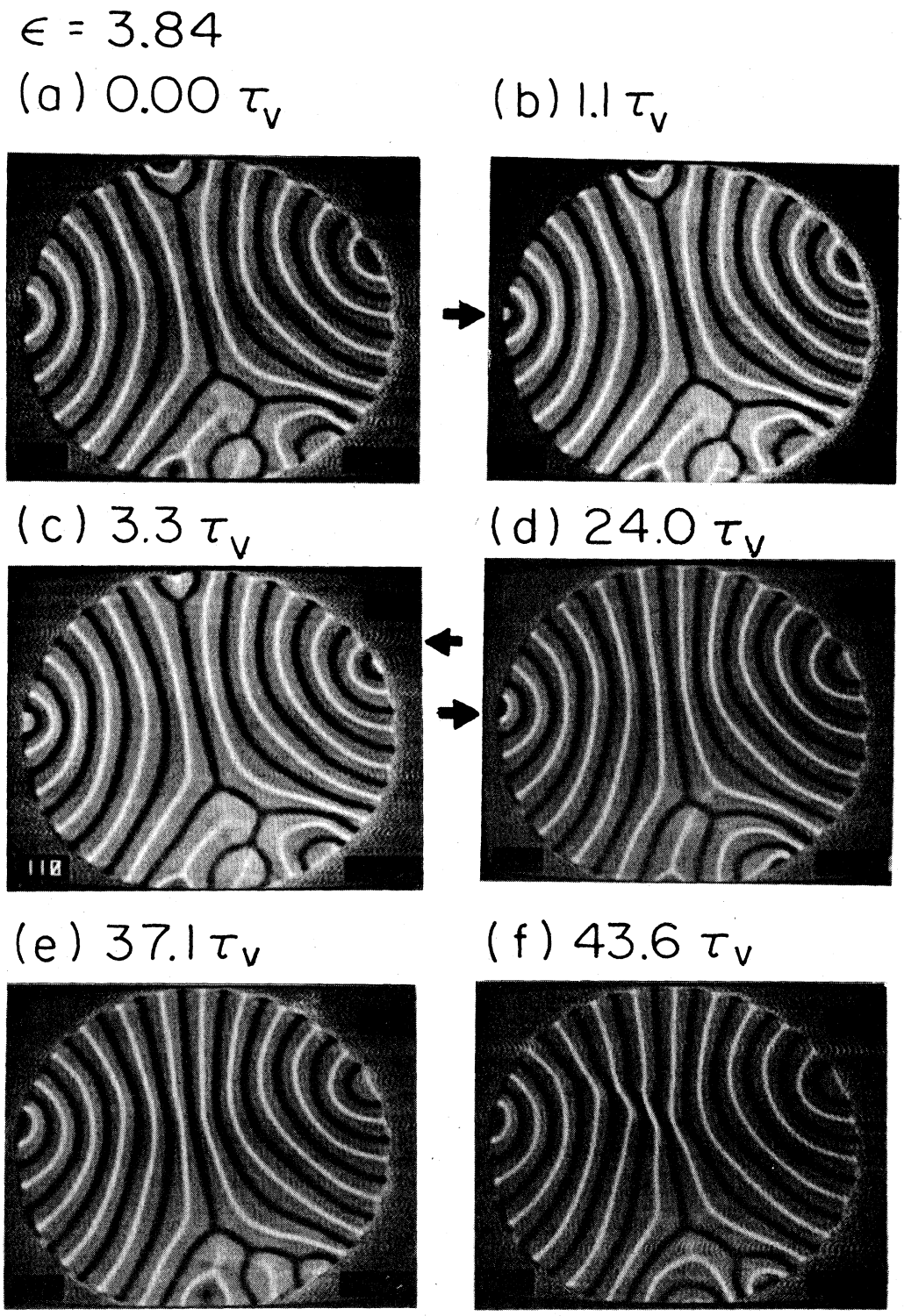

FIG. 11. Sequence illustrating time-dependent flow due to persistent roll nucleation far above onset, at $\epsilon=3.84$. (a)—(f) New rolls appear at the sidewall disclinations (arrows), and rolls in the center are pinched. (g)—(l) A pair of dislocations forms, eliminating one roll pair; the entire sequence then repeats nonperiodically.

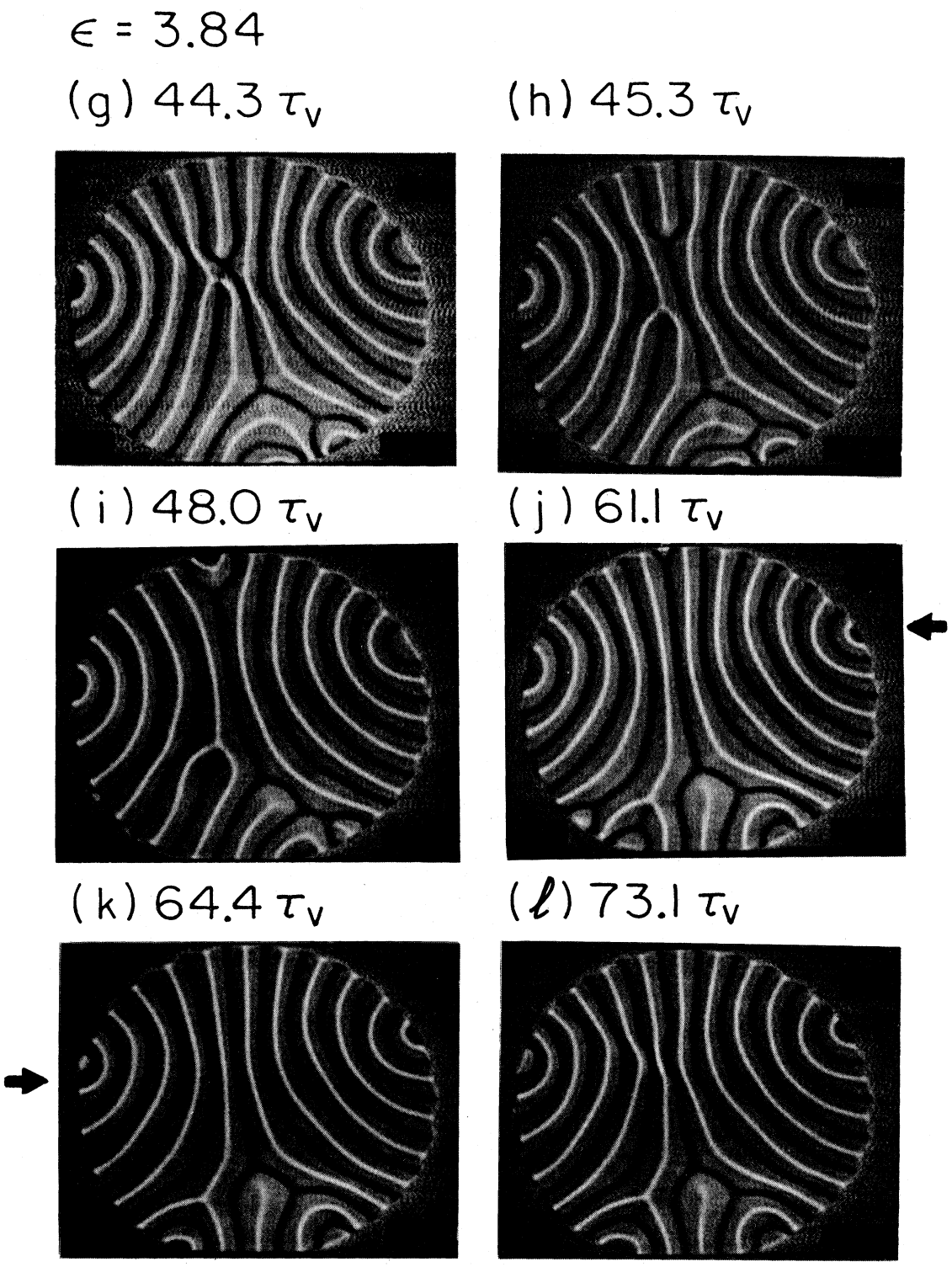

FIG. 11. (*Continued*).

the stable band, which is bounded by the cross-roll (CR) and skewed varicose (SV) instabilities at this ϵ. Finally, *far* from onset [for example, $\epsilon=3.64$, Fig. 15(c)] the pattern is again time dependent, and in this case much of $P(q)$ lies *above* the stable band, exceeding the SV instability threshold.

Data from many stable and time-dependent patterns are summarized in two ways in Figs. 16 and 17. Figure 16 shows the width σ of $P(q)$ for stable and time-dependent patterns, as well as the width Δ of the computed stable band, as a function of ϵ. The width of $P(q)$ (measured as the width of the central 80% of the distribution) does not

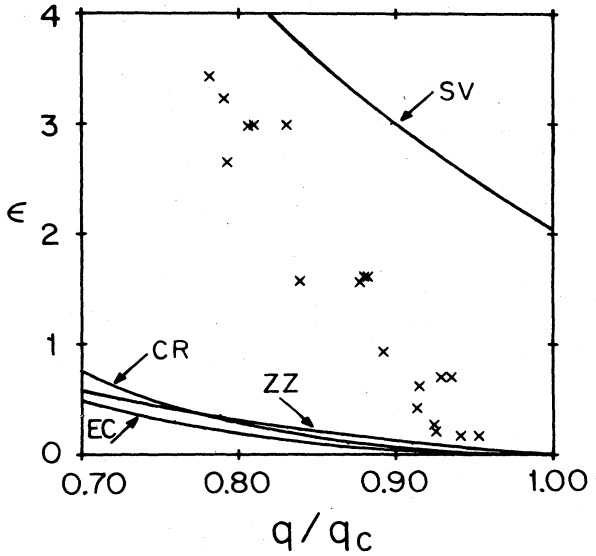

FIG. 12. Spatially averaged wave number $\langle q \rangle$ measured in stable textured patterns, for various ϵ. The thresholds of secondary instabilities at $P=2.5$ are shown by the solid lines.

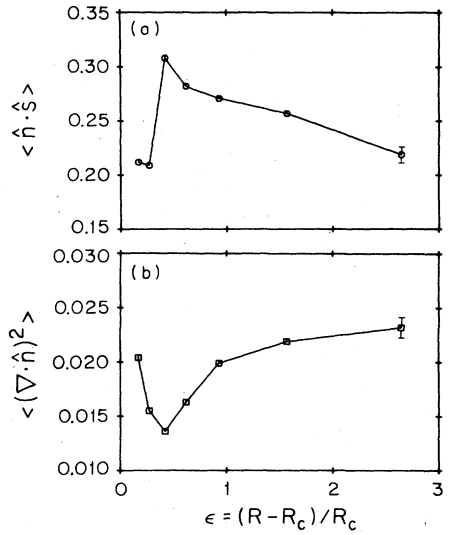

FIG. 14. Obliqueness and bending for one sequence of patterns formed by stepwise increments of ϵ. The behavior of this sequence at low ϵ violates the statistical trend seen in Fig. 13.

vary dramatically with ϵ, but tends to increase as ϵ increases. On the other hand, $\Delta \to 0$ rapidly as $\epsilon \to 0^+$, and after reaching a maximum at $\epsilon \approx 0.9$, Δ decreases slowly with increasing ϵ. The observed stable regime corresponds roughly to Δ being substantially larger than σ.

Figure 17 gives a more explicit comparison between $P(q)$ and the stable band, as a function of ϵ. Figure 17(a) shows the fraction f_- of $P(q)$ that lies below the lower boundary of the stable range. Only for $\epsilon < 0.4$ (approximately) does part of $P(q)$ lie below the stable range; the largest value of f_- were measured in time-dependent patterns at $\epsilon = 0.10$. The rise in this graph at low ϵ seems to be an indication of the onset of time dependence. Similarly, Fig. 17(b) shows the fraction f_+ versus ϵ. For $\epsilon > 3 f_+$ is large; the increase in f_+ seems to signal the loss of stability that occurs for $\epsilon > 3.5$.

By examining the wave-number field $q(\mathbf{r})$ we can see which areas of the pattern contain the unstable wave numbers. Figure 18(a) shows $q(\mathbf{r})$ for a time-dependent pattern *close* to onset ($\epsilon = 0.10$). Areas marked by vertical striping show where the local wavenumber lies below the zig-zag instability threshold ($q_{ZZ} = 0.91 q_c$ at $\epsilon = 0.10$ and $P = 2.5$). Roughly speaking, the roll spacing tends to be larger near defects and the sidewall, but the unstable wave

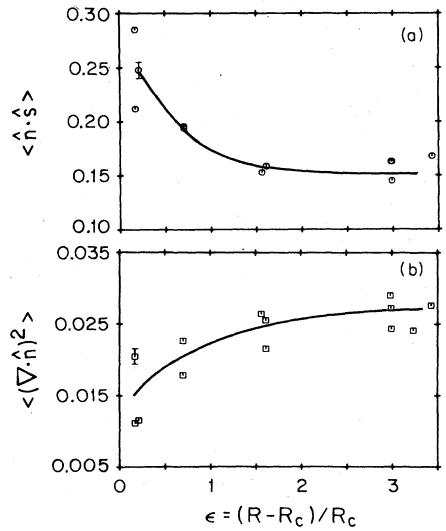

FIG. 13. Roll-sidewall obliqueness (a) and the roll bending (b), as a function of ϵ for many stable patterns. The statistical trend toward less obliqueness and greater bending is clear.

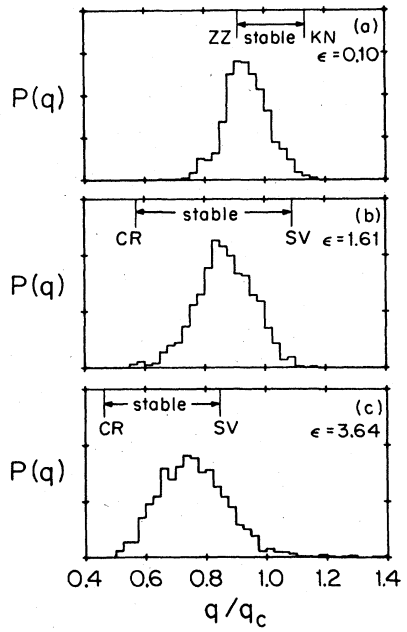

FIG. 15. Wave-number distribution $P(q)$ in patterns at several values of ϵ. The stable wave-number range is also shown. $P(q)$ lies within the stable band at moderate ϵ, but partially outside it at low and high ϵ.

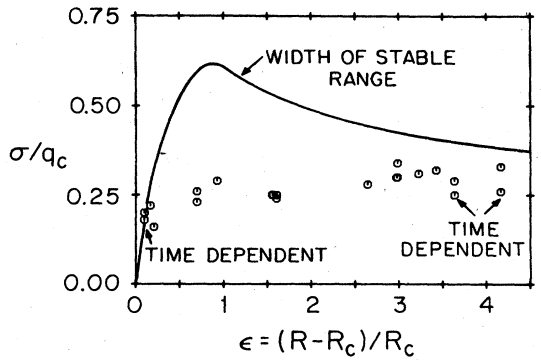

FIG. 16. Width σ of $P(q)$ and the width Δ of the stable band, as a function of ϵ. The regions where σ is comparable to Δ correspond qualitatively to time-dependent regimes.

numbers are not clearly localized.

In time-dependent patterns *far* from onset, compression of the rolls leads to turbulent evolution. Figure 18(b) shows $q(\mathbf{r})$ for a pattern at $\epsilon=4.17$, just prior to the formation of a pair of dislocations. Here the vertical striping indicates that $q>q_{SV}$ ($q_{SV}=0.81q_c$ at $\epsilon=4.17$ and $P=2.5$), and the entire central area of the pattern contains unstable wave numbers when the rolls are compressed. (The elimination of a roll pair significantly reduces the area where $q>q_{SV}$.)

3. *Transient pattern evolution and the Lyapunov functional*

We describe the behavior of the Lyapunov functional only briefly, since we have little to add to our previous report.[5] Figure 19 shows an example of the evolution of F and the three largest contributions to it, on a logarithmic time scale. The defect contribution F_D is estimated[5,22] from the number of disclinations in the pattern. However, one must assume a radius r_c over which the roll amplitude is suppressed. We use an intermediate value r_c equal to 1.6 times the ϵ-dependent correlation length ξ. However, we show a large shaded uncertainty in the total F; this arises from the fact that r_c could probably be as small as ξ or as large as 2ξ.

During the early phase of evolution (up to about $7\tau_h$ in this case), the evolution of F is consistent with a monotonic decline, mainly because F_D is large and decreasing (and has a large uncertainty). However, the slow wave-

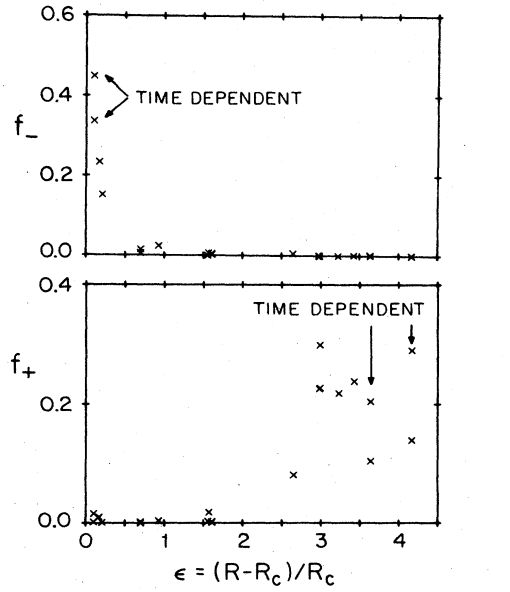

FIG. 17. Fractions f_- and f_+ of $P(q)$ below and above the stable band, as a function of ϵ. The rise in each of these graphs is a precursor of persistent time dependence.

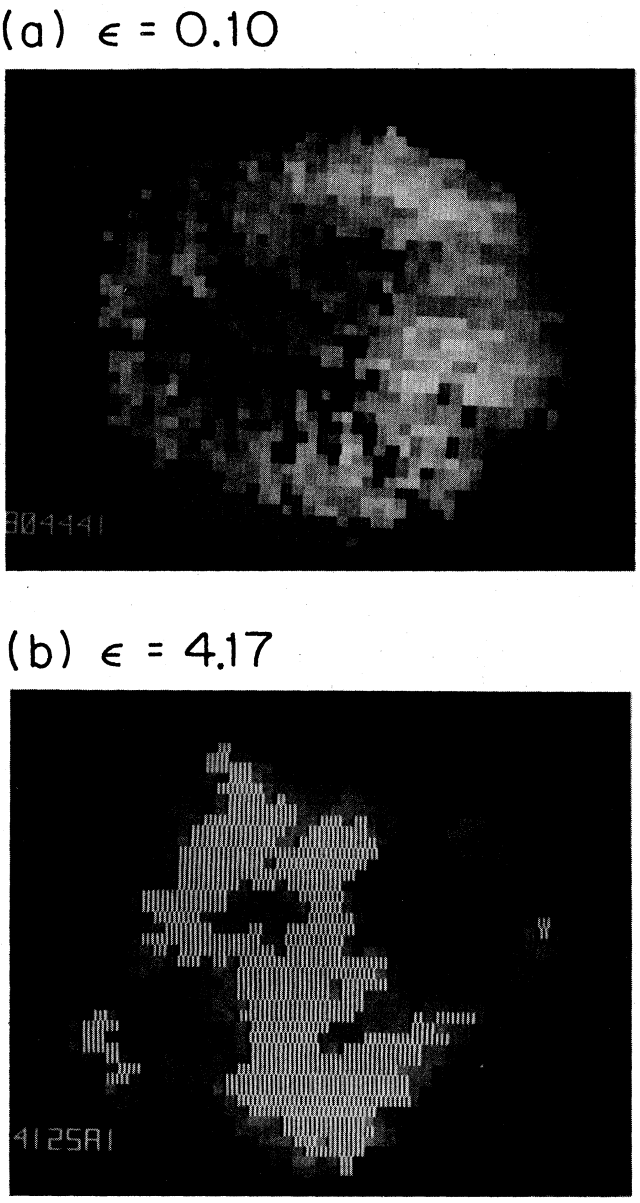

FIG. 18. Graphical display (vertically striped) of regions where the wave number is locally outside the stable band. These patterns are time dependent.

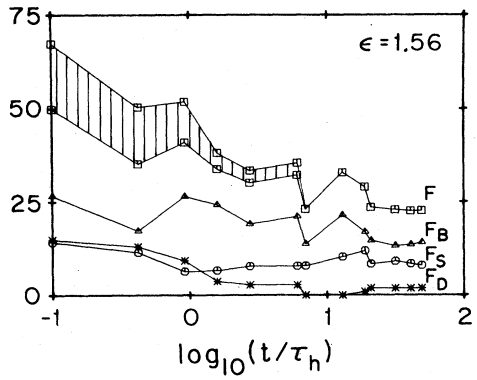

FIG. 19. Swift-Hohenberg Lyapunov functional as a function of time (logarithmically) at $\epsilon = 1.56$. The separate contributions due to the bulk (F_B), surface (F_S), and defects (F_D) are also shown. The origin of the uncertainty is explained in the text. Slow wavenumber adjustments at the end of this run lead to fluctuations in F.

number adjustment that occurs after most of the defects are eliminated [see Figs. 10(g) and 10(h)] leads to a short-term *increase* in F, due mostly to an increase in the value of the $(q-q_0)^2$ term in F_B. As an new defect pair forms on the sidewall [Figs. 10(i) and 10(j)], F decreases again. In some other runs, F is observed to be monotonic. To summarize, we find that in the range $\epsilon < 3.0$, F is either monotonic, or predominantly monotonic with small reversals. Farther from onset, nonrelaxational behavior becomes quite pronounced. Very *close* to onset, the time dependence of F becomes too small to measure.

The nonuniqueness of *stable* textured patterns is often reflected by different values of F. Figure 20 shows F as a function of ϵ in stable patterns. The variations in F at a given ϵ (up to 25%) arise mainly from differences in $F_{\delta q}$, which is the largest contribution in patterns containing few defects. The overall linear trend of F with ϵ results from the fact that $F_{\delta q} \propto \epsilon \int (q-q_0)^2 d^2r$, and the integral does not vary greatly with ϵ.

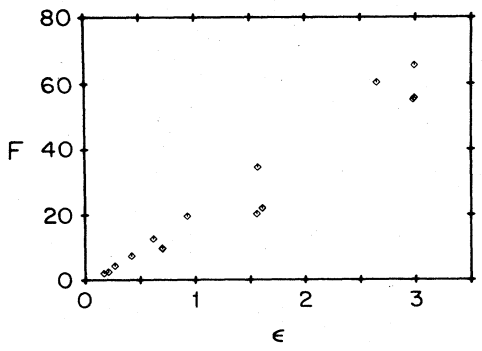

FIG. 20. Measured values of the Swift-Hohenberg Lyapunov functional as a function of ϵ for many stable patterns. The nonuniqueness of the patterns is sometimes reflected in F.

IV. DISCUSSION AND CONCLUSIONS

The wave-vector field $\mathbf{q}(\mathbf{r})$ provides a quantitative measure of the structure of stable and time-dependent textured convection patterns. This field can be measured with a precision of a few percent using digital image analysis. In this section we discuss the results of this study in comparison with theory and other experiments.

A. Form of stable patterns

The variations of the spatially averaged wave number $\langle q \rangle$ with ϵ are similar to previous results for textured patterns in a large rectangular cell.[24] Several theoretical approaches[10,25,26] have been applied to wave-number selection, especially in simple patterns, but these have not yielded a prediction of the properties of the mean wavenumber in textured patterns.

In many stable patterns the mean roll bending $\langle (\nabla \cdot \mathbf{n})^2 \rangle$ increases, and the mean roll-sidewall obliqueness $\langle \mathbf{n} \cdot \mathbf{s} \rangle$ decreases, as ϵ is increased. This trend has already been noted qualitatively.[4] It is also expected from the Swift-Hohenberg model, because the term in the Lyapunov functional that is proportional to $\langle (\nabla \cdot \mathbf{n})^2 \rangle$ scales with ϵ, whereas that proportional to $\langle \mathbf{n} \cdot \mathbf{s} \rangle$ scales with $\epsilon^{3/2}$. This means that boundary alignment will play a larger role than curvature in minimizing F at large ϵ. However, we have observed a sequence of patterns that clearly exhibits the *opposite* opposite behavior for $\epsilon < 0.5$ (Fig. 14). This behavior is still compatible with the model since other terms in F, especially that due to wave-number deviations, are often larger, so that the competition is generally not limited to the terms under discussion here.

The form of textured patterns may well depend on initial conditions or thermal history, in addition to the distance above onset. Finally, we remark that the distinct patterns that occur at a given ϵ are often found to have considerably different values of the Swift-Hohenberg Lyapunov functional.

B. Wave-number field and the onset of time dependence

1. Flows near onset

When $\epsilon < 0.2$ (approximately) the flow apparently never stabilizes. Instead, the slow and erratic propagation of grain boundaries through the pattern persists indefinitely. This unexpected phenomenon has been observed only recently,[9] because of its extremely slow time scale and because of difficulties in flow visualization close to onset.

One possibility we must address is that the time dependence close to onset may result from environmental fluctuations or experimental imperfections, such as inhomogeneities in the temperature control. Using the Swift-Hohenberg model as a guide, we note that the local minima defining stable states become extremely shallow near onset, so extrinsic effects can become significant. We are unstable to exclude these possibilities. However, in view of quite similar observations by Ahlers, Steinberg, and Cannell[9] (extending to about $200\tau_h$), it seems more likely

that the slow time dependence arises from intrinsic dynamics of the "ideal" system.

The existence of persistent time dependence close to onset is in *apparent* contradiction with well-established stability calculations[7,8] that predict straight rolls to be stable in a band of wave numbers that varies quadratically with ϵ. (Of course, these results are for an infinite layer.) The fact that the unstable patterns contain wave numbers outside the stable band may allow this behavior to be understood eventually. We infer from our observations that the stability calculations provide a useful guide to the stability of textured patterns in a finite system. However, this picture is not completely consistent with all of the observations: it is not clear how the onset of the zig-zag instability would lead to time dependence in the form of slow defect motions.

These observations raise a new question: Why is the wave-number distribution wider than the stable band in textured patterns close to onset? Perhaps model equations can be used to study the stability of flows in finite geometry in order to better understand this issue. It is possible that experiments at other values of the Prandtl number might help to clarify the influence of various secondary instabilities on flows near onset.

An alternate explanation for the onset of time dependence has been proposed recently by Cross, Tesauro, and Greenside,[28] who show in numerical simulations that competition between selection processes favoring different wave numbers can lead to oscillatory time dependence near onset. (They find, for example, that grain boundaries favor a different wave number than one-dimensional processes.) It is not clear how to test this hypothesis using our data.

Square cell. It is natural to ask whether the circular symmetry of the boundary is related to the persistent time dependence near onset. That is, would the same phenomenon occur in a rectangular geometry? We have tried to answer this question by conducting similar experiments in a square cell constructed to have the same aspect ratio as the circular one. (In this case, we use half the length of an edge in place of the radius in computing the aspect ratio.) Our longest run (at $\epsilon=0.07$) was still time-dependent after $50\tau_h$ but had clearly stabilized by $100\tau_h$. There is considerable variability from one run to the next. The only statement that we can confidently make is that stable states do *exist* near onset in a square cell. Whether they are generally realized (or "found") is still uncertain.

2. *Flows far from onset*

Now we comment on the qualitatively distinct time dependence that occurs for $\epsilon > 3.5$ via the repetitive nucleation of dislocation pairs. This type of destabilization has been observed in several previous experiments[3,27] and has been associated with the skewed varicose instability. Though this destabilization seems to be associated with a large value of f_+ (the fraction of the wave-number distribution $P(q)$ that exceeds the stable band), some patterns with large values of f_+ are stable. This phenomenon suggests that $P(q)$ does not tell the entire story.

C. Transient pattern evolution

From an empirical point of view, it seems that pattern evolution can be characterized in terms of defect motions and their influence on the wave-vector field. The spontaneous nucleation of dislocations during transients far above onset[5] is a dramatic example of the role of defects; the wave-number adjustment accompanying the slow evolution of defects at moderate ϵ is another. The interactions between defects and the wave-number field can lead to nonmonotonic evolution of the Swift-Hohenberg Lyapunov functional F.

Although a truly adequate model will probably be nonrelaxational, this simple model correctly describes some qualitative features of convective pattern formation, and has provided a useful guide to the development of quantitative methods that can be applied in experiments.

ACKNOWLEDGMENTS

This work was supported by the National Science Foundation under Grant No. MSM-83-10933 to Haverford College. We appreciate the assistance of Omar Cheema in obtaining results for the square convection cell.

[1]V. Croquette, M. Mory, and F. Schosseler, J. Phys. (Paris) **44**, 293 (1983).
[2]P. Bergé, in *Chaos and Order in Nature,* edited by H. Haken (Springer-Verlag, Berlin, 1981).
[3]J. P. Gollub, J. F. Steinman, and A. R. McCarriar, J. Fluid Mech. **125**, 259 (1982).
[4]V. Steinberg, G. Ahlers, and D. S. Cannell, Phys. Scr. T **9**, 97 (1984).
[5]M. S. Heutmaker, P. N. Fraenkel, and J. P. Gollub, Phys. Rev. Lett. **54**, 1369 (1985).
[6]P. Kolodner, R. W. Walden, A. Passner and C. M. Surko, J. Fluid Mech. **163**, 195 (1986).
[7]F. H. Busse and R. M. Clever, J. Fluid Mech. **91**, 319 (1979).
[8]E. W. Bolton, F. H. Busse, and R. M. Clever, J. FLuid Mech. **164**, 469 (1986).
[9]G. Ahlers, V. Steinberg, and D. S. Cannell, Phys. Rev. Lett. **54**, 1373 (1985).
[10]M. C. Cross and A. C. Newell, Physica (Utrecht) **10D**, 299 (1984).
[11]P. Manneville, J. Phys. (Paris) Lett. **44**, L-903 (1983).
[12]A. Zippelius and E. D. Siggia, Phys. Fluids **26**, 2905 (1983).
[13]Y. Pomeau and P. Manneville, J. Phys. (Paris) Lett. **40**, L-609 (1979).
[14]H. S. Greenside and M. C. Cross, Phys. Rev. A **31**, 2492 (1985).
[15]J. Swift and P. C. Hohenberg, Phys. Rev. A **15**, 319 (1977).
[16]H. S. Greenside and W. M. Coughran, Jr., Phys. Rev. A **30**, 398 (1984).

[17]M. C. Cross, Phys. Rev. A **25**, 1065 (1982).
[18]M. S. Heutmaker and J. P. Gollub, Physica D (to be published).
[19]W. Merzkirch, *Flow Visualization* (Academic, New York, 1974).
[20]V. Croquette (private communication).
[21]P. N. Fraenkel, Senior thesis, Haverford College, 1984 (unpublished).
[22]M. S. Heutmaker, Ph.D. thesis, University of Pennsylvania, 1986 (unpublished).
[23]M. L. James, G. M. Smith, and J. C. Wolford, *Applied Numerical Methods for Digital Computation* (IEP, New York, 1977).
[24]J. P. Gollub and A. R. McCarriar, Phys. Rev. A **26**, 3470 (1982).
[25]Y. Pomeau and P. Manneville, J. Phys. (Paris) **42**, 1067 (1981).
[26]J. C. Buell and I. Catton, Phys. Fluids **29**, 23 (1986).
[27]A. Pocheau, V. Croquette, and P. LeGal, Phys. Rev. Lett. **55**, 1094 (1985).
[28]M. C. Cross, G. Tesauro, and H. S. Greenside, Physica D (to be published).

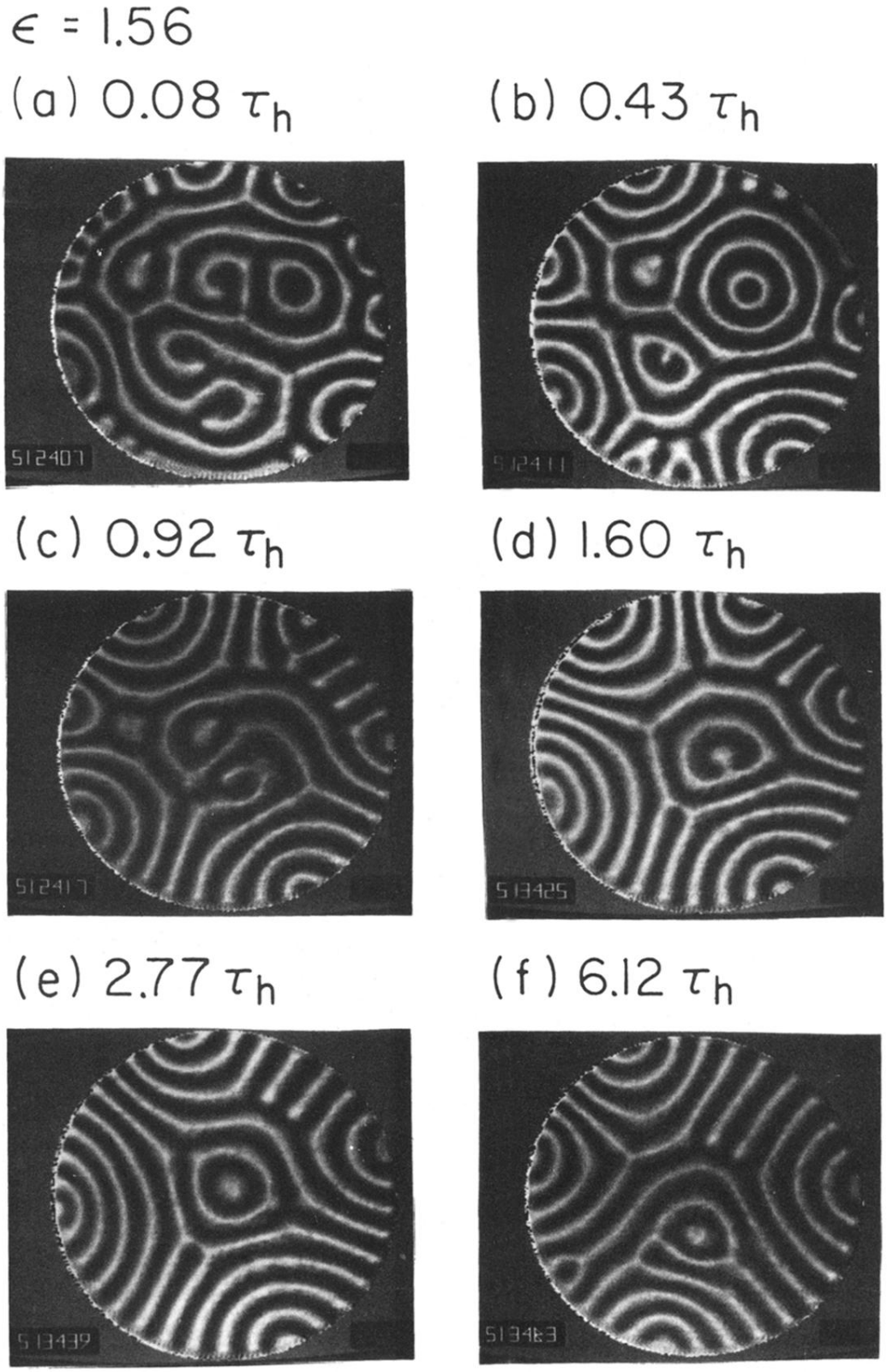

FIG. 10. Transient evolution sequence at $\epsilon = 1.56$. Large wave-number variations are visible as defects evolve.

$\epsilon = 1.56$

(g) $7.01\,\tau_h$

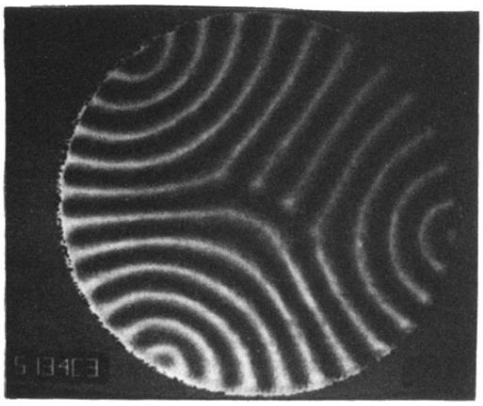

(h) $13.1\,\tau_h$

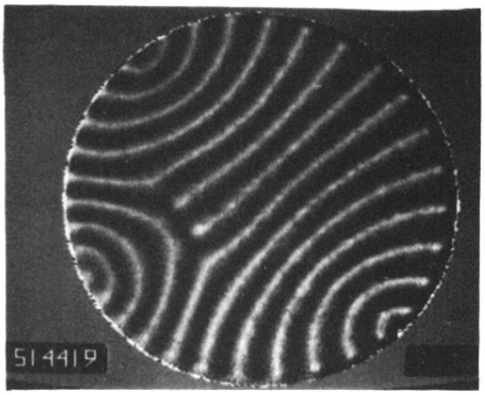

(i) $19.1\,\tau_h$

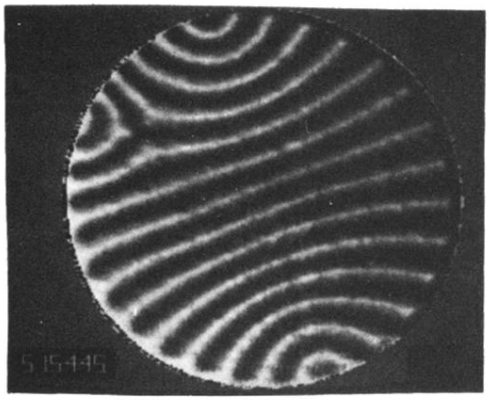

(j) $21.1\,\tau_h$

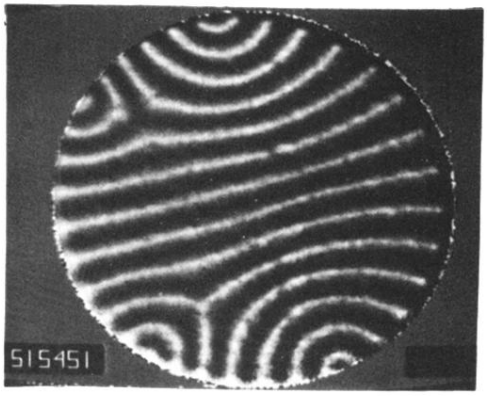

(k) $41.2\,\tau_h$

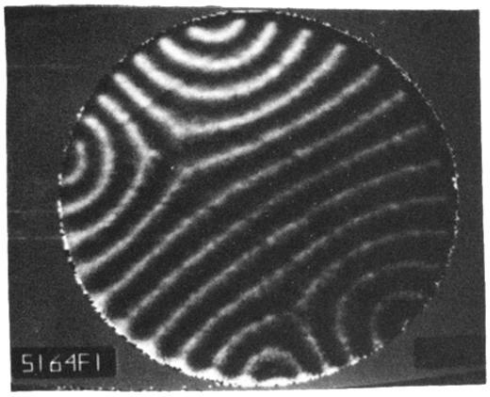

(ℓ) $49.7\,\tau_h$

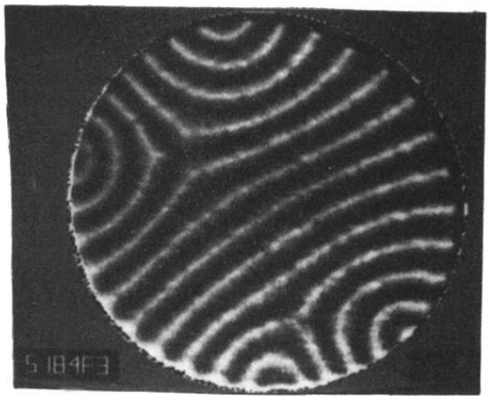

FIG. 10. (*Continued*).

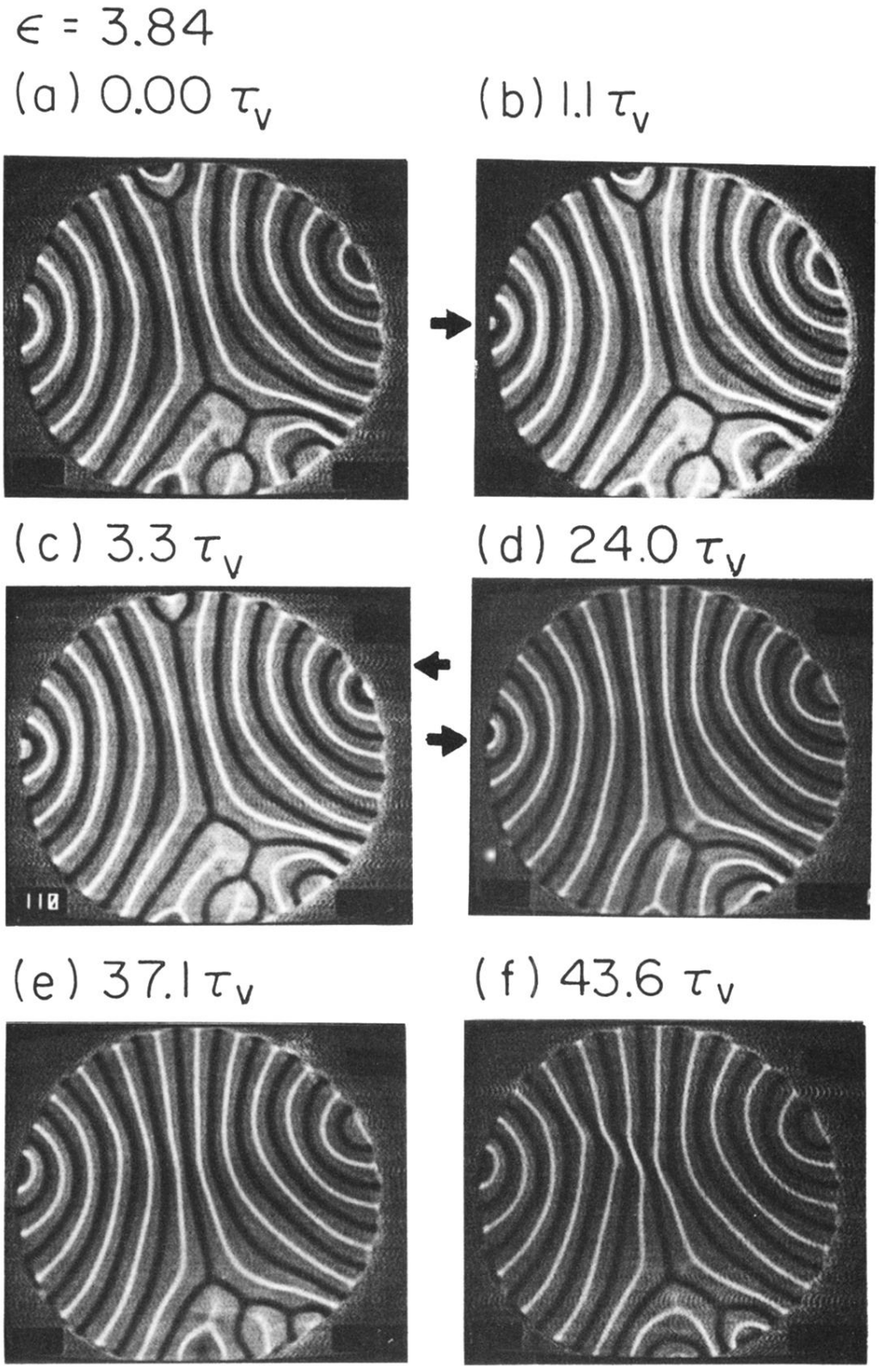

FIG. 11. Sequence illustrating time-dependent flow due to persistent roll nucleation far above onset, at $\epsilon=3.84$. (a)—(f) New rolls appear at the sidewall disclinations (arrows), and rolls in the center are pinched. (g)—(l) A pair of dislocations forms, eliminating one roll pair; the entire sequence then repeats nonperiodically.

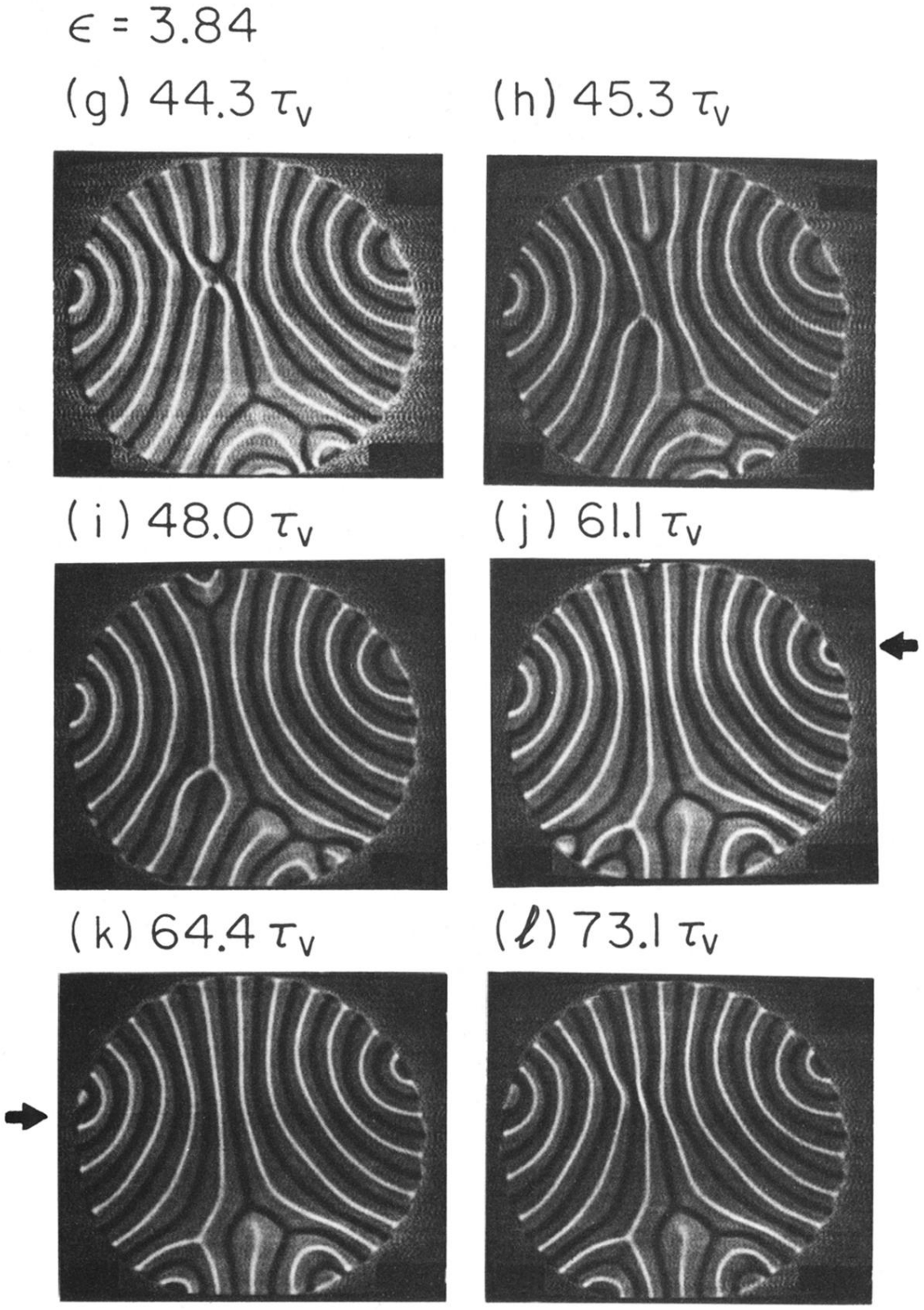

FIG. 11. (*Continued*).

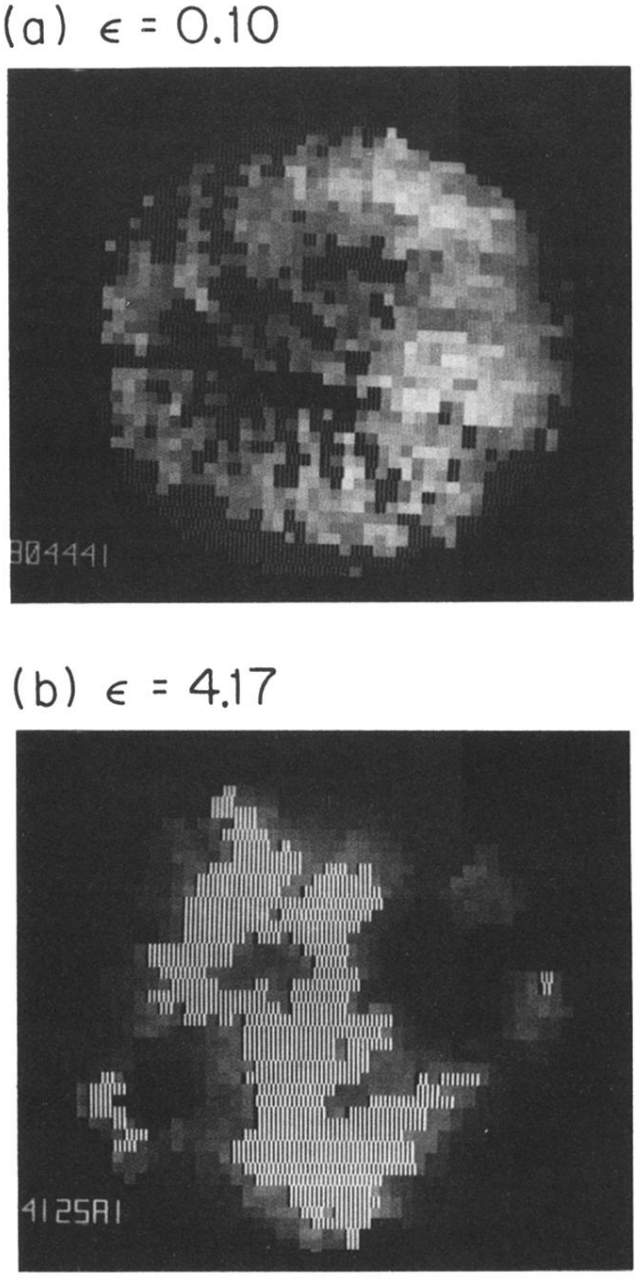

FIG. 18. Graphical display (vertically striped) of regions where the wave number is locally outside the stable band. These patterns are time dependent.

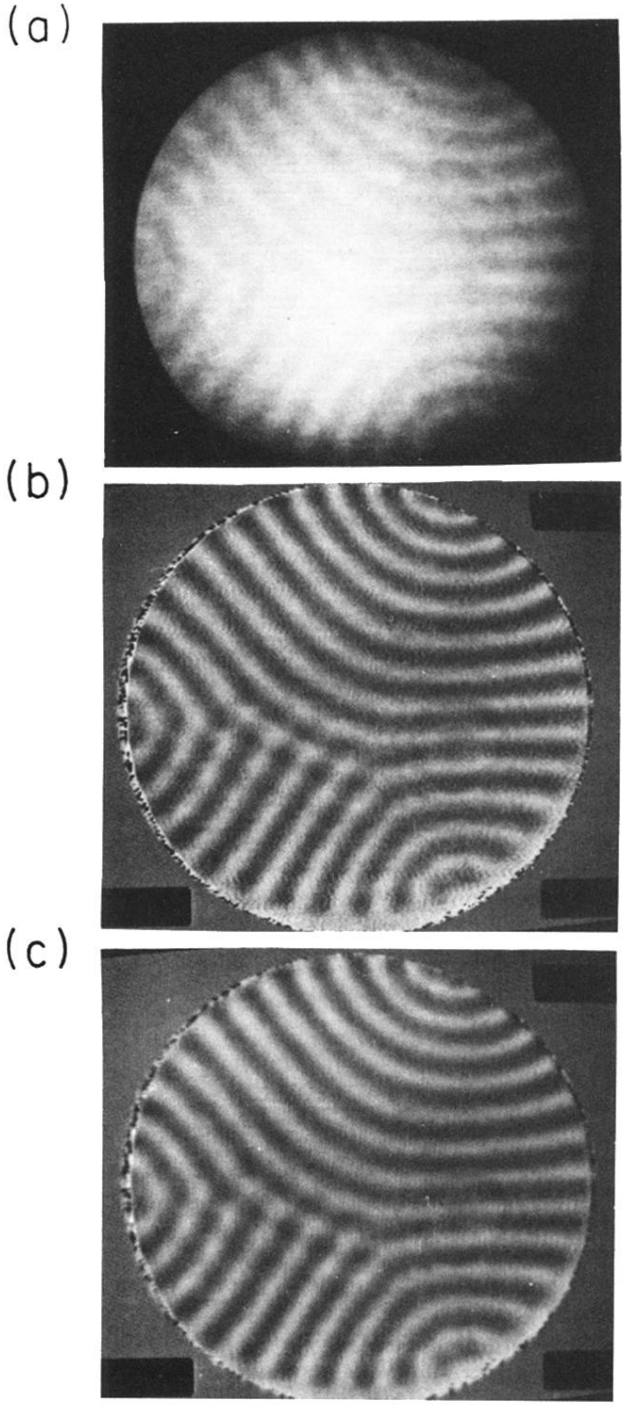

FIG. 3. Processing the shadowgraph by image division and smoothing. (a) Image (at $\epsilon=0.1$) formed by averaging 64 video frames; the contrast is weak and the illumination nonuniform. (b) Point-by-point division by a reference image with no convection improves uniformity and allows contrast to be enhanced. (c) Nearest pixel smoothing reduces small scale noise.

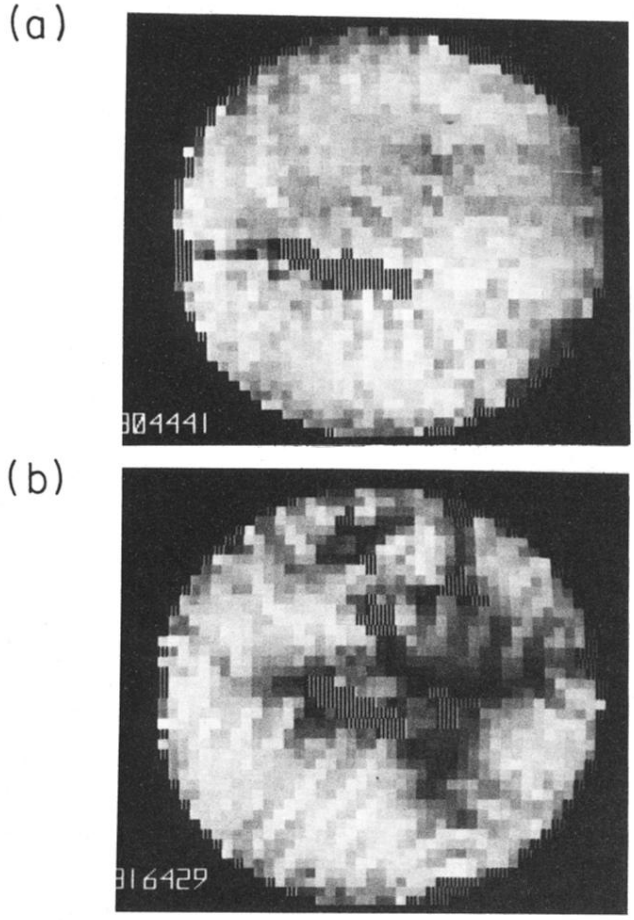

FIG. 7. Measured wave-number field $q(\mathbf{r})$ for the patterns of Fig. 4. The intensity of the grey scale is coded in proportion to the wave number; the field cannot be measured near the defects (vertically striped regions).

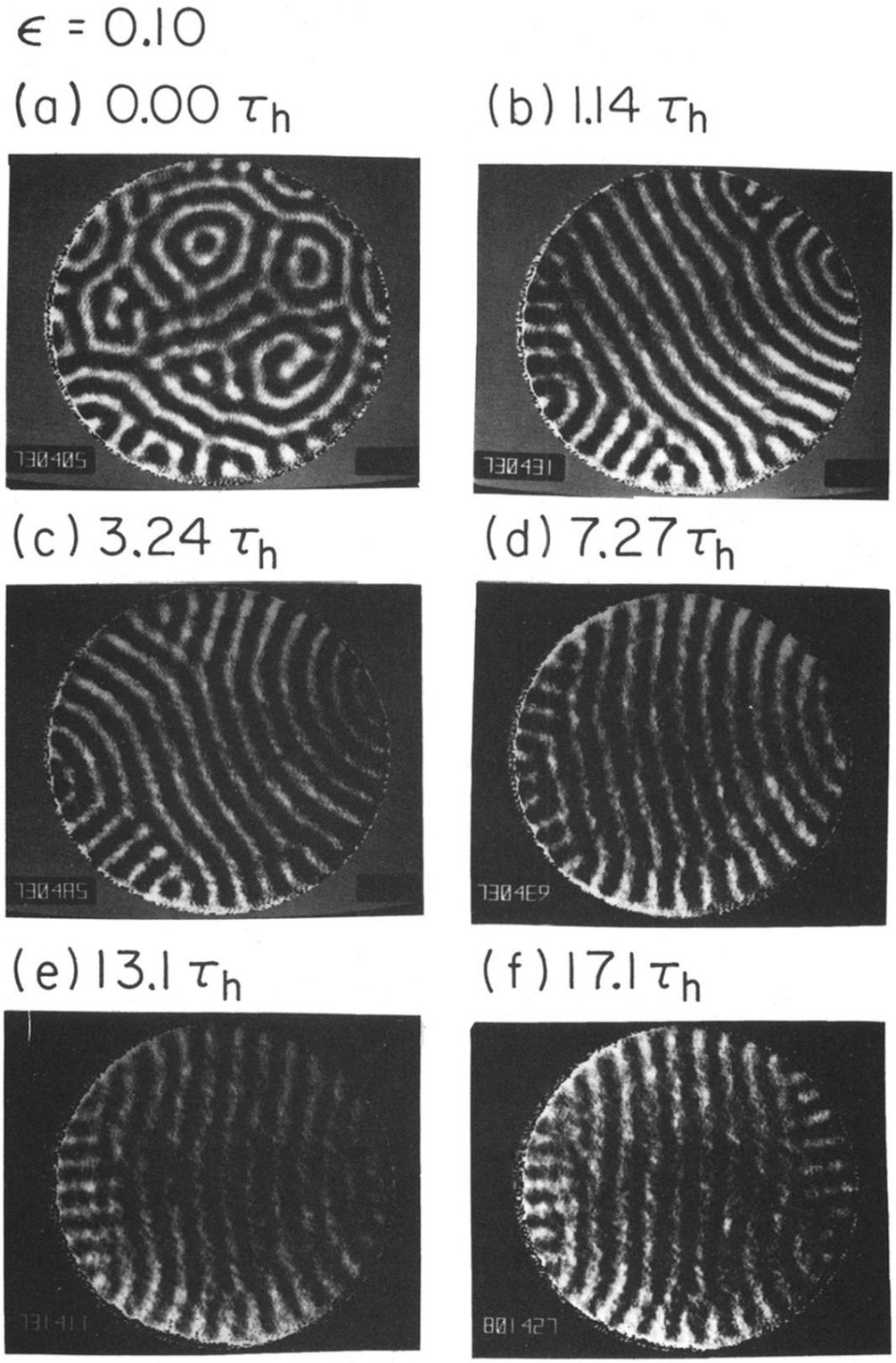

FIG. 8. Sequences of images at $\epsilon=0.10$ (10% above onset) showing persistent time dependence near the onset of convection. Times are given in units of the horizontal thermal diffusion time τ_h. Grain boundary motions persist throughout observations spanning $45\tau_h$.

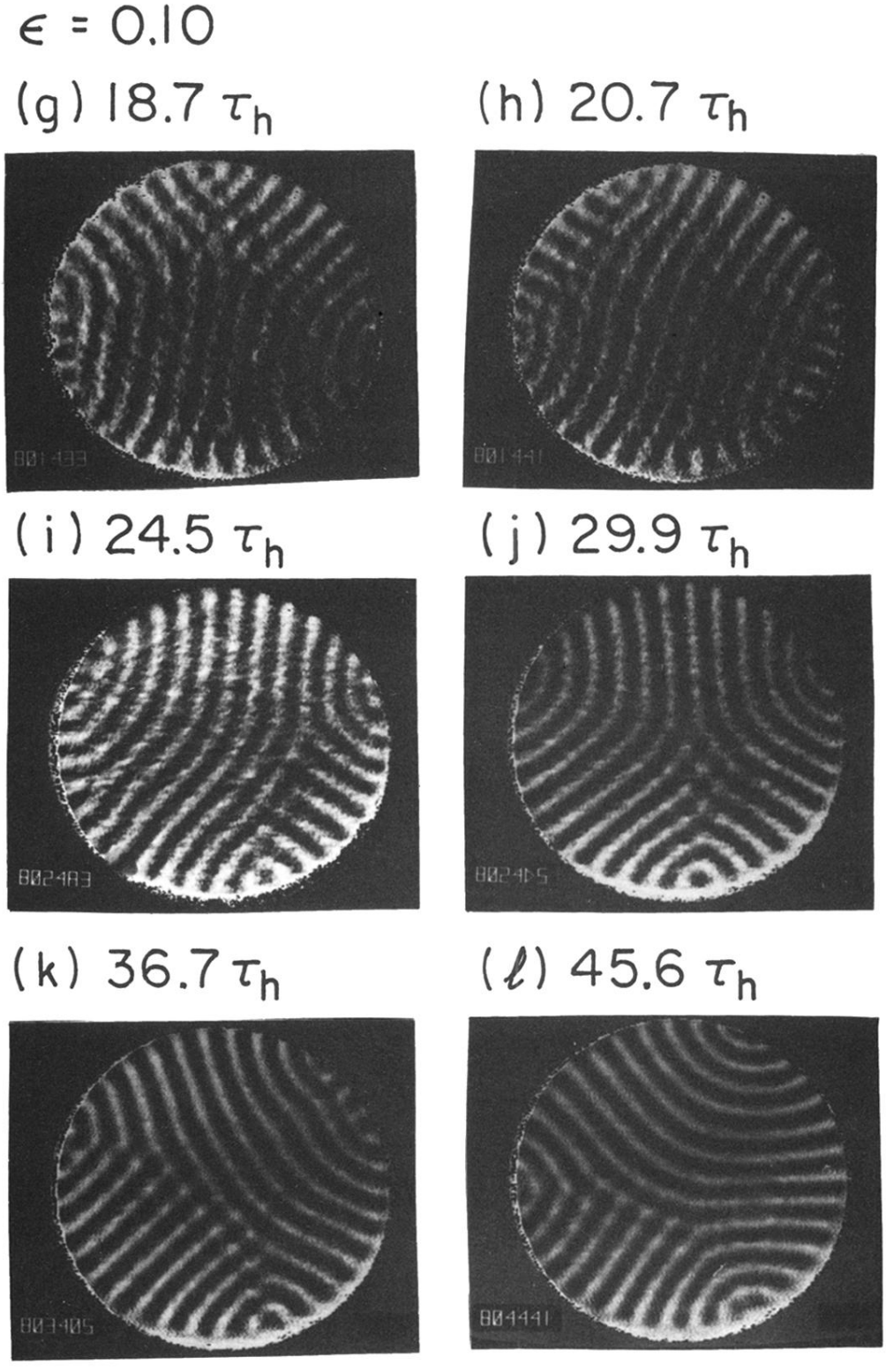

FIG. 8. (*Continued*).

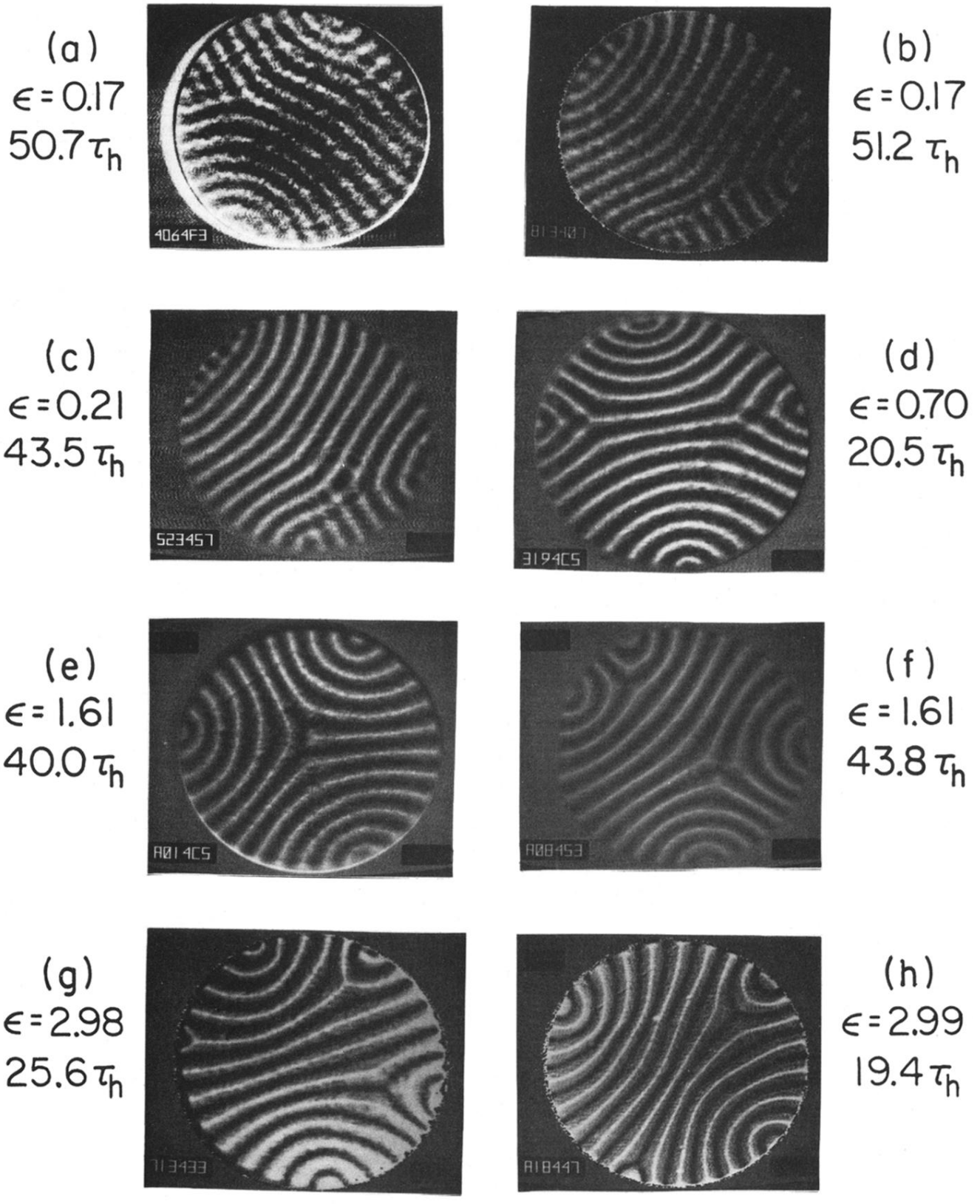

FIG. 9. Stable textured patterns formed at various ϵ. The patterns are not unique at a given ϵ: note (a) and (b); (e) and (f); and (g) and (h). The elapsed time is also shown.